Received: 29 October 2024 | Revised: 9 January 2025 | Accepted: 29 January 2025

DOI: 10.1002/cjce.25663

RESEARCH ARTICLE

THE CANADIAN JOURNAL OF CHEMICAL ENGINEERING

Analysis of flow regimes and volumetric phase fraction of vertical upward gas–liquid–solid three-phase flow

Ronaldo Luís Höhn | **Abderraouf Arabi** | **Sylvana Verónica Varela Ballesta** | **Paolo Juan Sassi** | **Jordi Pallarès** | **Youssef Stiriba**

Departament d'Enginyeria Mecànica, Universitat Rovira i Virgili, Tarragona, Spain

Correspondence
Youssef Stiriba, Av. Països Catalans 26, Tarragona, 43007, Catalonia, Spain.
Email: youssef.stiriba@urv.cat

Funding information
Ministerio de Ciencia e Innovación (MCIN), Grant/Award Numbers: PID2020-113303GB-C21, PID2023-146648NB-C21; Agencia Estatal de Investigación (AEI), Grant/Award Number: 2021SGR00732; the Departament de Recerca i Universitats de la Generalitat de Catalunya as well as from the European Union's Horizon 2020 research and innovation programme under the Marie Skłodowska-Curie, Grant/Award Numbers: 713679, 945413; the Martí Franquès COFUND Doctoral Programme; AA has received funding from the postdoctoral fellowships programme Beatriu de Pinós, Grant/Award Number: 2021 BP 00052; the Secretary of Universities and Research (Government of Catalonia); the Horizon 2020 Programme of Research and Innovation of the European Union under the Marie Skłodowska-Curie, Grant/Award Number: 801370

Abstract

Gas–liquid–solid flows are important in many industrial productions and processes. The hydrodynamic of gas–liquid–solid three-phase vertical upward flows and how the presence of solid particles may affect the two-phase flow system properties are less investigated and understood compared to gas–liquid two-phase flow. The present study is an attempt to bridge this gap in vertical pipe through an experimental investigation of flow regimes and volumetric holdup with solid particles less dense than liquid phase, similar to hydrates. The experiments are carried out using air–water and polypropylene pellets solid particles and a 30 mm ID vertical pipe. Three solid volumetric concentrations (5%, 10%, and 20%) were investigated, and the results are compared with those obtained with gas–liquid two-phase flow. In the conditions of experimental measurements carried out, four flow regimes, namely cap bubble-to-slug, slug, churn, and dispersed bubble flows, were reported. These flow regimes were observed on both two-phase and three-phase flow conditions. Meanwhile, the injection of solids induced a shift of slug-to-churn flow transition. The study allows notably to prove that the existing predictive models of flow transition and liquid holdup developed for two-phase flow can be extended to three-phase flow by considering the gas–liquid–solid three-phase as gas–slurry two-phase flow.

KEYWORDS

gas–liquid-two-phase flow, gas–liquid-solid three-phase flow, vertical upward flow, volumetric fraction

1 | INTRODUCTION

Gas–liquid upward two-phase flows in vertical pipes are common in many industrial applications, including oil and gas production, heat exchangers, and nuclear thermo-hydraulic plants, as well as for the transportation of multiphase fluid mixtures over long distances or processing products.[1–4] An important characteristic of this type of flow is the presence of several interfacial configuration shapes, referred to as flow regimes, which result from different forces acting on the flow and depend on the physical properties of the two-phase flow system and operating conditions.

They influence both global and local hydrodynamic parameters and heat, as well as mass transfer phenomena.[5–8]

In vertical upward flow, we typically identify five main flow regimes: bubbly, slug, churn, annular, and dispersed bubbles,[9–12] and under certain experimental conditions, a cap bubble flow pattern can also appear between bubbly and slug flows.[13] Accurately describing these regimes is necessary for many global predictive and closure relations models.[14,15] Therefore, to predict the range of parameters for each flow regime and characterize the global interfacial structure, transition models have been developed based on pipe geometry, superficial velocities, and the physical properties of both phases.[10] Furthermore, several predictive models have been developed to estimate liquid holdup (H_l) or gas holdup, which is also referred to as void fraction (α). These models can be classified into four correlation categories: slip ratio, $K\alpha_H$, drift flux, and general gas or liquid holdup. Details about this classification can be found in the literature.[16,17] These cited references also highlighted the difficulty of estimating this parameter. Table 1 summarizes the existing models.

Conversely, the additional presence of solid particles in gas–liquid systems is common in the minerals industry, where airlift pumps transport solid particles such as sand or small stones.[27] In the oil and gas industry, it occurs when sand particles are entrained[28] or when the hydrates form.[29,30] Solid particles might also appear in a hypothetical severe accident in the nuclear industry.[31] The interactions between the three phases in gas–liquid–solid flow are more complex than those in gas–liquid two-phase flow. Indeed, the presence of solid particles may modify the dynamics of bubble collisions, breakup, and coalescence, leading to alterations in the flow characteristics, including flow regime transitions.[32–35]

Due to the complexity of gas–liquid–solid three-phase flows, most of the literature studies employed models and correlations based on gas–liquid two-phase flow, assuming that the solid–liquid slurry flow behaves as a single pseudo-homogeneous flow.[28,33,34,36] The advantage of this approach lies in the utilization of acquired knowledge about gas–liquid two-phase flows, which are comparatively more studied and better understood. Furthermore,

TABLE 1 Liquid holdup correlations considered for this study.

References	Volumetric fraction correlation
Nicklin[18]	$H_l = 1 - \frac{J_g}{1.2(J_g+J_l)+0.35\sqrt{gD}}$
Chisholm[19]	$H_l = \left(1-\left(1+X^{0.8}\right)^{-0.378}\right)$
Rouhani and Axelsson[20]	$H_l = 1 - \frac{x}{\rho_g}\left[C_0\left(\frac{x}{\rho_g}+\frac{1-x}{\rho_l}\right)+\frac{U_{GM}}{G}\right]^{-1}$ $U_{GM} = \left(\frac{1.18}{\sqrt{\rho_l}}\right)\left(g\sigma\left(\rho_l-\rho_g\right)\right)^{0.25}$ $C_0 = 1+0.2(1-x)(gD)^{0.25}\left(\frac{\rho_l}{G}\right)^{0.5}$
Bonnecaze et al.[21]	$H_l = 1 - \frac{J_g}{1.2(J_g+J_l)+0.35\sqrt{gd}\left(1-\frac{\rho_g}{\rho_l}\right)}$
Beggs and Brill[22]	$\frac{H_l}{H_{l(0)}} = 1 + C\left[\sin(1.8\theta) - \frac{1}{3}\sin^3(1.8\theta)\right]$
Huq and Loth[23]	$H_l = \frac{2(1-x)^2}{1-2x+\left[1+4x(1-x)\left(\frac{\rho_L}{\rho_g}-1\right)\right]^{0.5}}$
Woldesemayat and Ghajar[16]	$H_l = 1 - \frac{J_g}{C_0(J_g+J_l)+u_{gu}}$ $C_0 = \frac{J_g}{J_g+J_l}\left[1+\left(\frac{J_L}{J_g}\right)\left(\frac{\rho_g}{\rho_l}\right)^{0.1}\right]$ $u_{gu} = 2.9(1.22+1.22\sin\theta)^{p_{atm}/p_{sym}}\left[\frac{gD\sigma(1+\cos\theta)(\rho_l-\rho_g)}{\rho_l^2}\right]^{0.25}$
Armand—Massena	$H_l = 1 - (0.833+0.167x)\left(1+\frac{1-x}{x}\frac{\rho_g}{\rho_l}\right)^{-1}$
Kanizawa and Ribatski[24]	$H_l = 1 - \left[1+14.549\mathrm{We}_m^{-0.222}\left(\frac{\mu_l}{\mu_g}\right)^{-1.334}\left(\frac{\rho_g}{\rho_l}\right)^{1/3}\left(\frac{1-x}{x}\right)^{2/3}\right]^{-1}$
Almabrok et al.[25]	$H_l = 1 - J_g\left[1.028\left(J_g+J_l\right)+0.35\left(\frac{g\sigma\left(\rho_l-\rho_g\right)}{\rho_l^2}\right)^{0.5}\right]^{-1}$
AlSaif and Al-Sarkhi[26]	$H_l = 1 - \frac{J_g}{\left\{1.0011\left(\left(J_g+J_l\right)+3.9771\left[\sin\left(\frac{\pi}{90}\theta\right)+1\right]\left[\frac{g\sigma(\rho_l-\rho_g)}{\rho_l^2}\right]^{0.25}\right)\right\}}$

TABLE 2 Previous studies of gas–liquid–solid flow in vertical pipelines.

Research	Pipe dimensions	Phases	Solid parameters	Main contribution
Hatate et al.[39]	Vertical upward I.D = 15.5, 25.9 mm	Air Water Glass	$d_s = 30, 60, 100\ \mu_m$ $\rho_s = 2.52\ g/cm^3$ $H_{sl} = 0\%$ to 65%	Effect of solid concentration, gas holdup, and pressure drop measurements
Sakaguchi et al.[41] Sakaguchi et al.[40]	Vertical upward I.D = 20.9, 30.6, 50.8 mm	Air Water Aluminium ceramics	$d_s = 1.15, 2.56$ 4.16 mm $\rho_s = 2380\ kg/m^3$ 2270, 2400 kg/m^3 $J_s = 0.00429$ to 0.0635 m/s	Model for three-phase slug pressure drop and volumetric fraction empirical nondimensional equation
Yoshinaga and Sato[42]	Vertical upward I.D = 26, 40 mm	Air water Ceramic/resin	$d_s = 6.1, 9.9, 6.0, 9.5$ $\rho_s = 2540, 3630\ kg/m^3$ $J_s = 0$ to 0.14 m/s	Triangular relationship between the air and water flow rate and particles discharged
Douek et al.[32]	Vertical upward & Downward I.D = 0.08 m	Air Water Glass	$d_s = 500, 600\ \mu_m$ $\rho_s = 2550\ kg/m^3$ $H_s = 0.02$ to 0.15	Drift flux model for three-phase flow with the inclusion of phase interaction terms
Hatta et al.[43]	Vertical upward I.D = 18/18 mm 18/22 mm, 20/28 mm	Air Water Glass	$d_s = 0.0052$ m $\rho_s = 2500\ kg/m^3$ $J_s = 0.009$ to 0.016 m/s	Numerical treatment for mixtures in vertical pipes with a sudden enlargement
Fujimoto et al.[27]	S-shaped pipes Vertical Upward I.D = 18 mm	Air water Alumina	$d_s = 3$ mm $\rho_s = 3600\ kg/m^3$ $J_s = 0.003$ m/s	Effects of S-shaped bends on airlifting
Erian and Pease[44]	Vertical upward I.D = 5, 10 cm	Air Water Sand	$d_s = 610, 1700$ 4800 μ_m $\rho_s = 2730\ kg/m^3$	Model calculation for pneumatically scarified solid particles
Kassab et al.[45]	Vertical upward ID = 25.4 mm	Air Water Limestone	$d_s = 4.75, 7.1$ 9.5, 11.3 mm $\rho_s = 2427\ kg/m^3$ $J_s = 0.025, 0.063$ m/s	Modified model to predict the airlift pump performance
Hosokawa et al.[31]	Vertical upward I.D = 30.3 mm	Air Water Aluminium ceramics	$d_s = 1.45, 3.19$ 4.16 mm $\rho_s = 2400\ kg/m3$ $H_s = 0.24\%$ to 1.6%	Liquid velocity measurement, turbulence intensity, and turbulence modification on three-phase flow
Takano et al.[46]	Vertical upward I.D = 26 mm	Air Water Resin balls	$d_s = 6$ mm $\rho_s = 1356\ kg/m^3$ $J_s = 0.041$ to 0.13 m/s	Correlations for frictional pressure drop in three-phase vertical flow

the flow regimes and hydrodynamic phenomena encountered are similar to those in two-phase flow.[33–35,37] Following this method, the physical properties of the slurry flow replace those of the liquid phase. The density of the slurry mixture, ρ_{sl}, is calculated from Equation (1):

$$\rho_{sl} = \rho_l(1 - H_s) + \rho_s H_s \quad (1)$$

where H_s, ρ_s, and ρ_l represent the solid volumetric fraction, the solid density, and the liquid density, respectively. According to Thomas,[38] the slurry viscosity, μ_{sl}, is

dependent on solid concentration and liquid viscosity, μ_l as follows:

$$\mu_{sl} = \mu_l \left[1.0 + 25H_s^2 + 0.062\exp\{1.875H_s/(1-1.595H_s)\}\right] \quad (2)$$

Experimental studies on vertical gas–liquid–solid pipe upward flow have been relatively underexplored in the literature. Table 2 presents a survey of relevant experimental studies in terms of pipe dimensions, fluids used, solid characteristics, the investigated hydrodynamic parameters, and the main results obtained from each study. For instance, Hatate et al.[39] reported that the gas holdup is independent of pipe diameter, particle diameter, and solid concentration. The authors verified that the two-phase volumetric fraction model proposed by Nicklin[18] also offers good agreement with the observed values of their three-phase data. Miller and Cain[37] studied the hydrodynamics of gas–liquid–solid vertical upward flow in a 5 cm ID pipe for four solid concentrations (0%, 5%, 10%, and 40%). The authors identified four flow regimes: bubble, bubble-slug (cap bubble), slug, and churn flow patterns. Miller and Cain[37] observed that the presence of solid particles shifts the bubble-to-cap bubble, and cap bubble-to-slug flows transition to lower gas superficial velocities. The increasing solid concentration induces a larger area covered by the cap-bubble flow pattern. This phenomenon was explained by the fact that the increase in solid concentration changes the apparent slurry viscosity, leading to an increase in bubble coalescence. The slug-to-churn flow transition was not impacted by the presence of a solid phase. For the gas holdup, the authors reported that the solid concentration influenced the radial distribution parameters differently for cap-bubble and slug flows. Sakaguchi et al.[40] focused only on bubbly flow and reported that the liquid holdup decreases with the increase in both solid concentration and particle diameter. Douek et al.[32] also observed that the presence of solid particles induces an increase at the bubble coalescence. These authors reported that the drift velocity of the gas phase is strongly impacted by the gas holdup.

We also noted that most research studies involve particles denser than the liquid phase. Furthermore, experimental studies with particles less dense than the liquid phase are scarce, as stated recently by Rosas et al.[33,47] and Sassi et al.,[34] who conducted studies in horizontal configurations. In this case, the particles, such as hydrates, are always carried by the liquid phase and they do not sediment. The presence or absence of solid particle sedimentation impacts local and global hydrodynamic parameters differently. Thus, the findings reported for vertical gas–liquid–solid flow, summarized in Table 2, cannot be applied directly to this type of three-phase flow. This statement highlights the necessity to perform experiments in this special case of three-phase flow.

This paper aims to fill the existing gap in vertical upward gas–liquid–solid three-phase flow through a new experimental study using polypropylene particles, of sizes ranging between 1 and 3 mm, less dense than the liquid phase similar to gas hydrates and already employed in our previous works Sassi et al.[34,35] The study primarily focuses on the influence of solid particles at different concentrations on various hydrodynamic flow parameters. We will present flow visualization analysis and discuss the results obtained regarding flow regimes, flow regime transitions, and liquid holdup.

2 | EXPERIMENTAL FACILITY

2.1 | Test facility and measurement methods

Experimental measurements were conducted in the low-pressure multiphase flow loop experimental facility built at the Mechanical Engineering Department at the ECoMMFiT laboratory. This facility was previously utilized by Sassi et al.[34,35,48] and Höhn et al.[49] to investigate the hydrodynamics of two-phase and three-phase flows at horizontal and vertical upward pipe orientation. Figure 1 shows a simplified schematic diagram of the vertical test section.

The flow loop facility is composed of horizontal, vertical upward, and vertical downward test sections of 30 mm ID straight transparent acrylic pipes connected by 90° vertical bends with a radius of curvature of 219.9 mm. The vertical upward test sections have 35 diameters in length, with a previous segment of 60 diameters and an addition of 17 diameters upstream to minimize flow disruption caused by the upstream and downstream bends. We refer the interested reader to our previous works[34,35,48] for a complete description.

The gas phase is air-compressed, previously filtrated, and dried from the laboratory manifold at a pressure of 6 bar. The air pressure was maintained by a reduction valve before being injected into the horizontal pipeline. An Omega mass flowmeter controller, with an accuracy of ±0.8%, regulates the gas superficial velocity in the experimental facility. Tap water was the liquid phase, and the solid phase was polypropylene pellets with a density of $\rho_s = 866\,\text{kg/m}^3$, diameters between 1 to 3 mm, and a maximum packing density of $C = 0.585$. The volumetric concentration was measured after submerging them in ethanol ($\rho_{\text{ethanol}} = 789\,\text{kg/m}^3$).

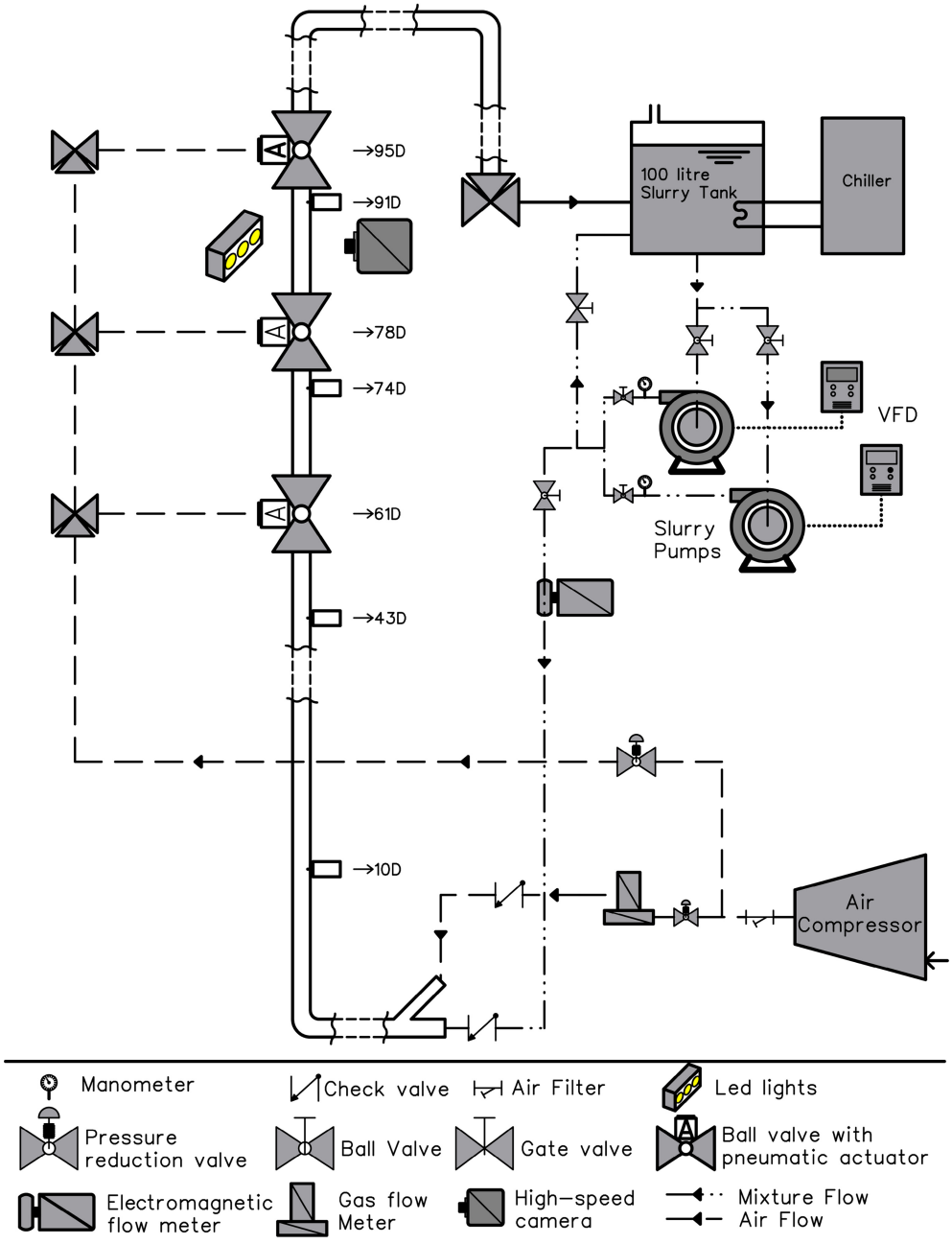

FIGURE 1 Schematics of experimental setup.

The gas and liquid/slurry phases were injected through a "Y" inlet junction, where gas entered the upper part and mixed with the liquid or slurry phase. The water or slurry–liquid phase was pumped by a 5.5 kW Weir AB80 centrifugal slurry pump. The water and polyethylene particles were added to the 100-litre tank in a specific concentration (5%, 10%, or 20%). A recirculation line with a globe ball valve was used to increase the turbulence inside the 100-litre tank and improve the homogeneity of the slurry phase. In the three-phase flow measurements, initial quantifications were performed to verify the solid concentration in the slurry tank. Subsequently, an additional verification of the solid concentration was conducted for liquid–solid flow on the test section through the quick-closing valve system (see Figure 1).

The average volume fraction of each phase was measured by simultaneously closing quick-closing ball valves. These valves closed simultaneously in 120 ms, and each valve had the same internal diameter as the acrylic pipeline. The volume fraction of the liquid and slurry phases trapped was extracted and measured after the air had disengaged from the water/slurry mixture. Each test condition has the liquid or slurry holdup values measured independently at least 5 times where the liquid/slurry and gas phases injection were stable for 2 min. The holdup

Flow type	C_s (%)	Test conditions	J_l (m/s)	J_g (m/s)
P	0%	66	0.75–3.5	0.2–7.0
P-5%	5%	56	0.75–3.5	0.2–7.0
P-10%	10%	27	0.75–3.0	0.2–7.0
P-20%	20%	29	0.75–3.0	0.2–7.0

TABLE 3 Test conditions.

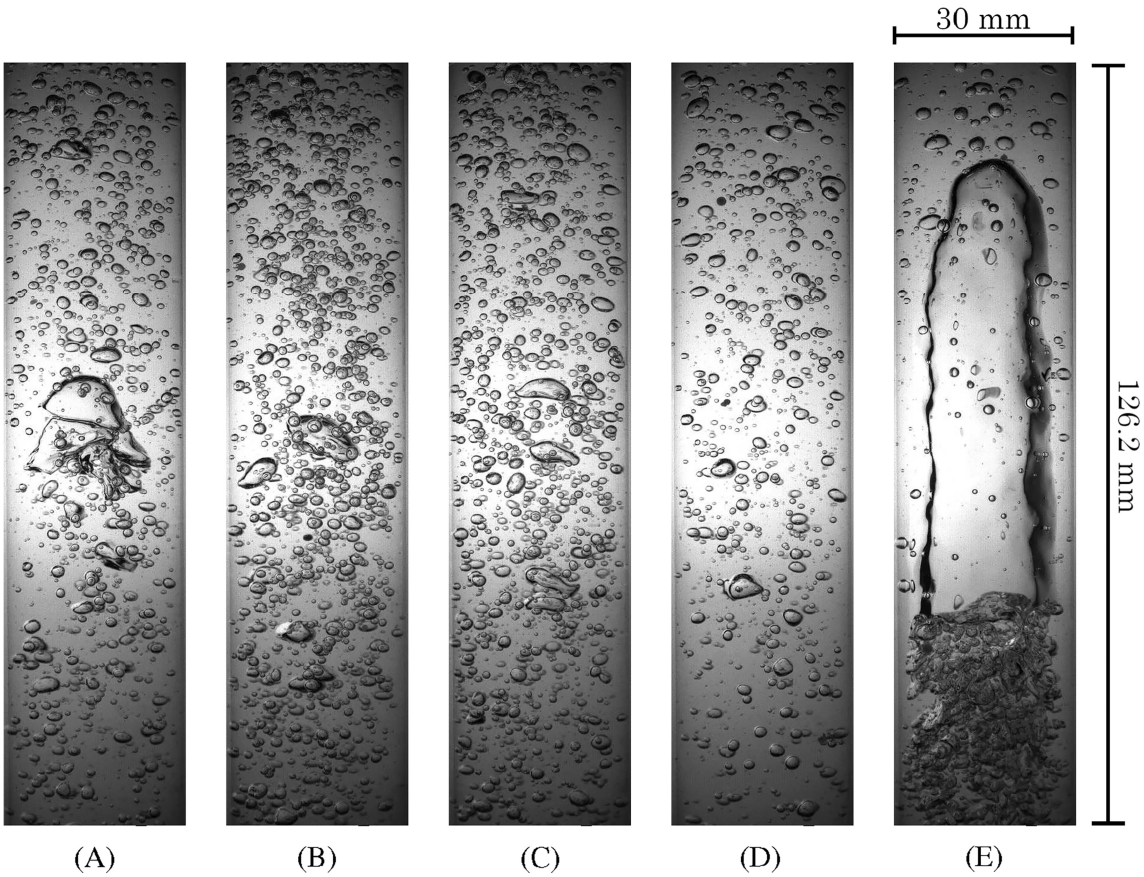

FIGURE 2 Different flow structures of two-phase cap-bubble to slug flow transition of $J_g = 0.20$ m/s and $J_l = 1.50$ m/s.

results for each test case were obtained by averaging these measurements. The standard deviations were found to be dependent on the flow conditions and ranged between 1.7% and 12.7%. Examples of the different carried-out measurements, the average, and the associated uncertainty are summarized in Appendix A, Table A1.

The flow visualization utilized a Photron Mini UX100 high-speed camera. Each study case was carefully visualized and analyzed by recording up to 5 s at 3200–4400 frames per second (FPS) to identify the different flow regimes. The applied FPS variation depended on the visualization of different flow patterns and/or the amount of particles present in each test condition. White LED backlight illumination combined with white diffusive screens was used to homogenize the light in the focus plane and achieve optimal illumination.

2.2 | Test condition

The test conditions were focused on different flow regimes, including cap bubble-slug, slug, churn, and dispersed bubble flows, the transition process between different regimes, and interfacial and local flow structures. A total of 66 two-phase test conditions were performed, with liquid superficial velocities ranging from 0.75 to 3.5 m/s and gas superficial velocities ranging from 0.2 to 7 m/s. Additionally, 56 three-phase flow conditions with 5% solid concentration, 27 test conditions with 10%, and 29 cases with 20% solid concentration were measured. The gas superficial velocities were kept in the same range as the two-phase flow cases, and 3.0 m/s was applied as the maximum of the liquid superficial velocity. Table 3 summarizes the ranges of superficial velocities and solid concentrations (C_s) for each test condition.

It should be noted that the two higher solid concentrations, combined with increased superficial gas and liquid velocities, raise pump power demands for proper phase homogenization and escalate the risk of particle damage. Consequently, the flow rate ranges for the 10% and 20% solid cases are narrower than in the other flow configurations.

3 | RESULTS AND DISCUSSION

The experimental data obtained from the cases presented in Table 3 are analyzed and discussed in this section. This experimental campaign aimed to achieve two main objectives: (1) to perform a flow visualization study to identify different flow regimes and represent the transition regions and limits caused by different solid concentrations and (2) to measure the volumetric fraction and compare it with available models in the open literature. For each selected test condition, we first present two-phase flows and discuss their characteristics, and then we discuss the effects of adding solid particles, following the order of increasing concentration, on the slurry flow by comparing the two- and three-phase flow results.

3.1 | Statistical analysis of the modelled flow parameters

As previously mentioned, the predictions of liquid holdup and slurry holdup obtained with the correlations of Table 1 were compared with the experimental data. The performance of these correlations were evaluated with three statistical parameters: Average percentage difference (APD) between the predicted and measured volumetric fractions, average absolute percentage difference (AAPD), and root mean square percentage difference (RMSPD). The three statistical parameters are defined by the following:

$$\mathrm{APD} = \frac{1}{n}\sum_{k=1}^{n}\left[\frac{\mathrm{Cal.}-\mathrm{Exp.}}{\mathrm{Exp.}}\right]\times 100 \tag{3}$$

$$\mathrm{AAPD} = \frac{1}{n}\sum_{k=1}^{n}\left|\frac{\mathrm{Cal.}-\mathrm{Exp.}}{\mathrm{Exp.}}\right|\times 100 \tag{4}$$

$$\mathrm{RMSPD} = \sqrt{\frac{1}{n}\sum_{k=1}^{n}\left[\frac{\mathrm{Cal.}-\mathrm{Exp.}}{\mathrm{Exp.}}\right]^{2}}\times 100, \tag{5}$$

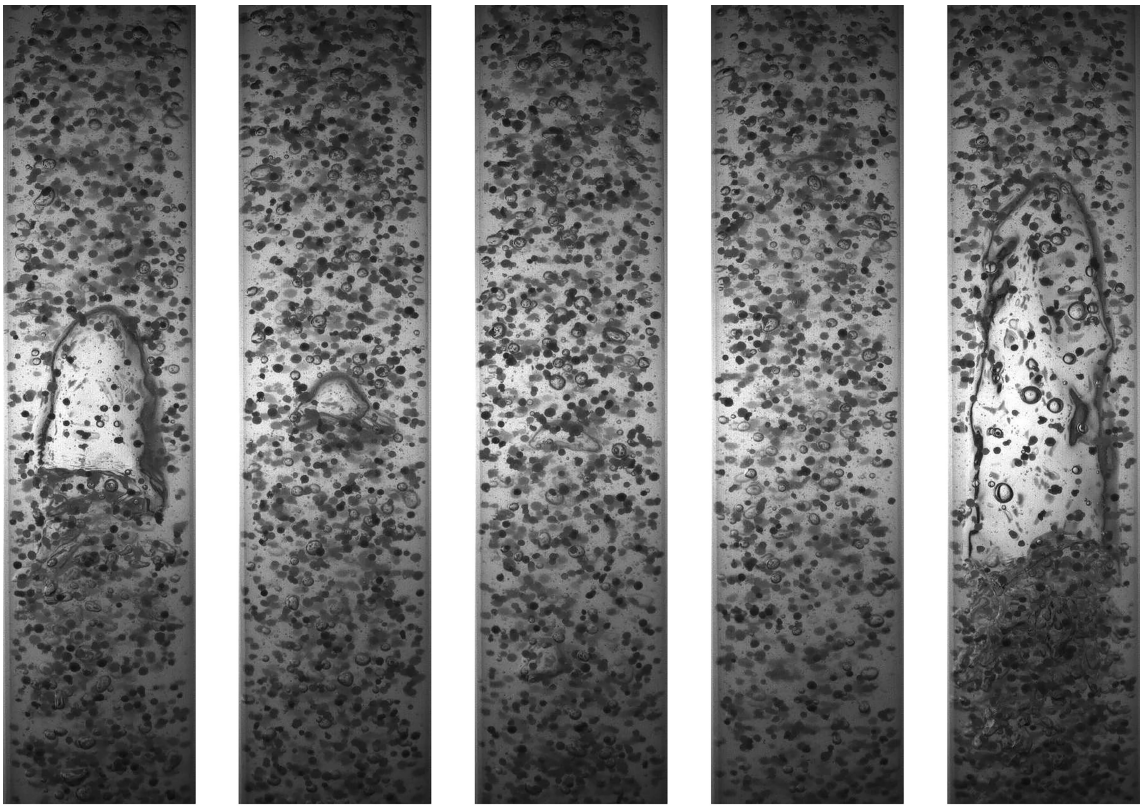

FIGURE 3 Different flow structures of three-phase $C_s = 5\%$ cap-bubble to slug flow transition of $J_g = 0.20$ m/s and $J_l = 1.50$ m/s.

in which the variables Cal. and Exp. can represent the volumetric fractions (H_l,H_{sl}).

3.2 | Flow pattern visualization

The flow visualization and identification of the experimental flow patterns were classified using a high-speed camera positioned at 90D length on the vertical test section (see Figure 1). The well-known works of Taitel et al.[9] and Shoham[50] were followed for the identification of flow structures and flow regimes. It was observed that the presence of particles in the gas–liquid flow affects some characteristics of the flow pattern. However, a similar categorization of flow regimes may be applied to gas–liquid–solid flow patterns, where the particles do not deposit due to gravity, so the sedimentation phenomenon is not present in flows with polyethylene particles. Furthermore, the liquid phase acts as a carrier phase for the solid phase. In our previous measurements,[34] we made similar considerations for flow visualization in a horizontal pipe.

The superficial velocities of the gas J_g and the liquid J_l ranged from 0.2 to 7 m/s and 0.75 to 3.5 m/s, respectively. In these conditions, the visualized flow patterns were cap bubble-slug, slug, churn, and disperse bubble. It was also possible to observe the transitions and the diverse sub-regimes from these flow patterns.

Dominant cap-bubble flow pattern cases were observed at low gas and liquid superficial velocities. For the gas–liquid test case with $J_g = 0.20$ m/s and $J_l = 1.50$ m/s, the geometric distribution of cap-bubbles was more recurrent, (see Figure 2A). Some characteristics and a more detailed classification of this flow pattern are detailed by Abdulkadir et al.[51] and Arabi et al.[13] It was usually considered as a transition from bubble to slug flow since it occurs at a relatively low gas flow rate. Taitel et al.[9] demonstrated that the transition from bubble to slug flow pattern happens when the gas holdup exceeds 0.25. Hence, the cap bubble may occur before this gas holdup is reached. During the experimental measurements and for the dominant cap-bubble regime, Taylor bubbles were also observed (see Figure 2E). It was also noted that there were regions with high concentrations

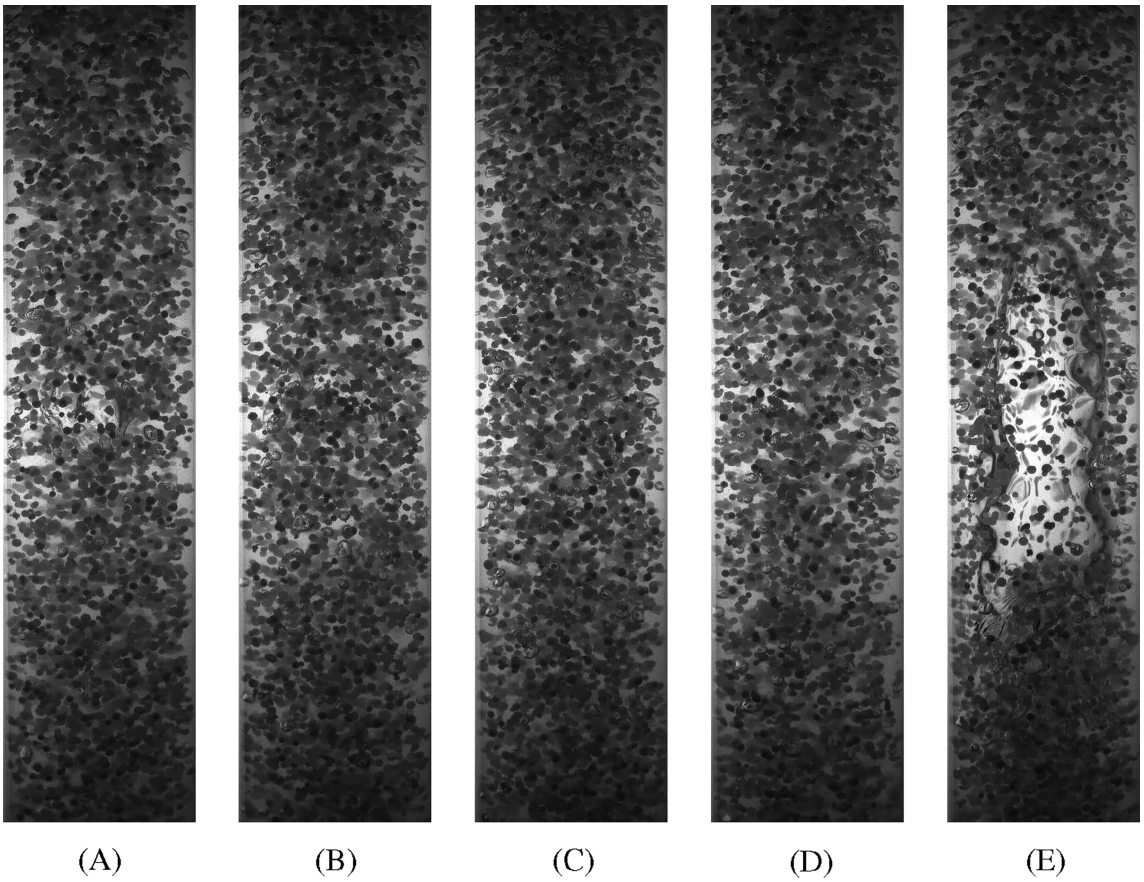

FIGURE 4 Different flow structures of three-phase $C_s = 10\%$ cap-bubble to slug flow transition of $J_g = 0.20$ m/s and $J_l = 1.50$ m/s.

of bubbles, as shown in Figure 2B. These clusters of bubbles include non-spheric bubbles of different sizes (see Figure 2C). The formation of cap flow patterns is due to the increased collisions and coalescence of bubbles as the gas injection grows, leading to the formation of bubble clusters and subsequent into cap bubbles. These cap bubbles are usually smaller than one diameter in length, do not occupy all the cross-sections of the pipe, and are not able to promote slugging.[50] A section with a low amount of dispersed bubbles was observed right after the passage of cap bubbles or in front of Taylor bubbles (see Figure 2D).

As solid particles were introduced at $J_g = 0.20$ m/s and $J_l = 1.50$ m/s, similar characteristic regions were visualized, as shown in Figure 3 corresponding to 5% of particles. However, the number of free bubbles was dramatically reduced, and it turns out the differences between the regions with a high and low amount of free bubbles decreased significantly, as shown in Figure 3B,C. Most of the gas transportation happens in the form of cap bubbles and Taylor bubbles, with a noticeable increase in the number of cap bubbles (see Figure 3A,E). These same effects were observed for 10% of solids, and the characterization of free bubble zones with different aerations becomes challenging (see Figure 4C,D). The visualization of elongated bubbles and cap bubbles increases, with a tendency toward the dominant slug flow pattern (see Figure 4A,E). With the increase in solid concentration to 20% of particles, the visualization of this flow pattern becomes more complicated due to the high amount of particles in the images (see Figure 5). There is no longer the presence of a high-aired region with a considerable number of bubbles of multiple sizes (see Figure 5D). The length of the longer bubbles decreased, and elongated bubbles were more frequent than the cap bubbles (see Figure 5E). Additionally, the cap and elongated bubble shape had more oscillations and sharp edges (see Figure 5A). The presence of bubbles was significantly reduced. This might be associated with the volume of particles occupied and/or due to the increase in bubble coalescence, as also reported by Douek et al.[32]

As the gas flow rate increases, the slug flow pattern is observed. This flow might be divided into two characteristic sections: the slug liquid and the elongated bubble, as shown in Figure 6 for the condition of $J_g = 0.50$ m/s and $J_l = 0.75$ m/s. The elongated bubble is formed due to the escalation of collisions and coalescence that increases

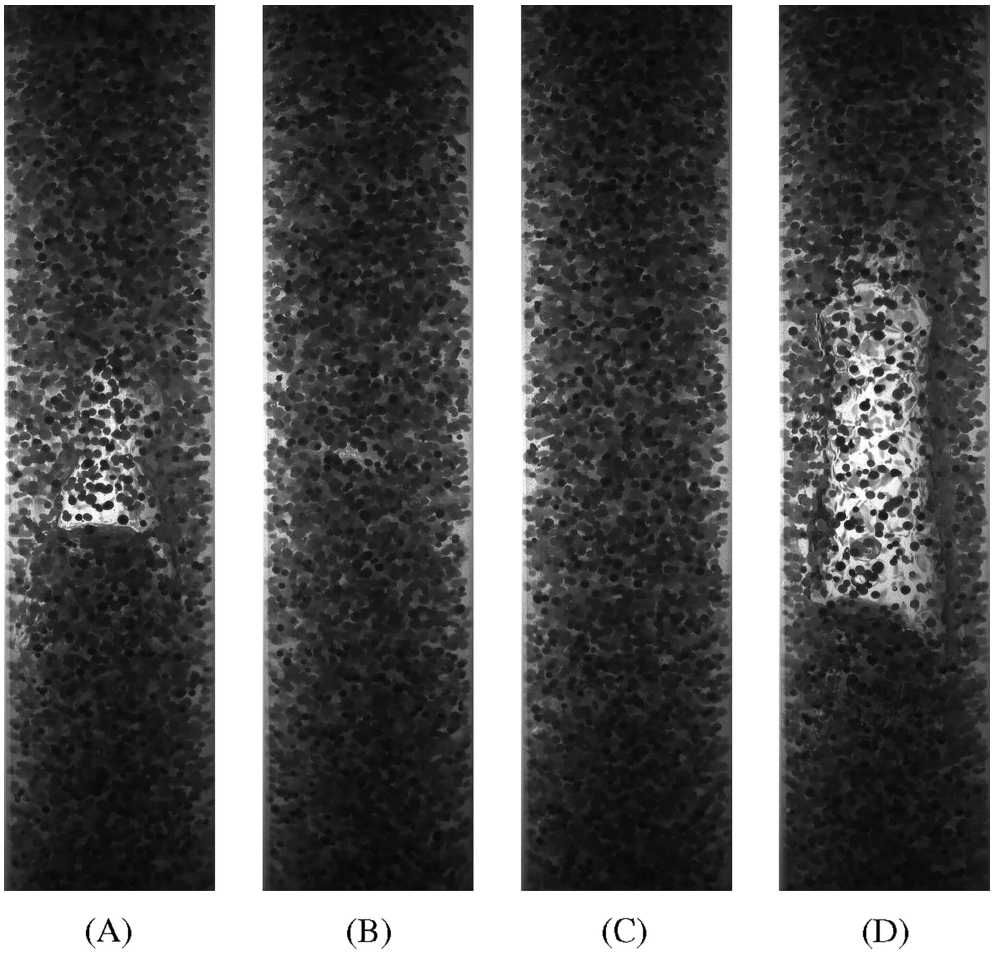

FIGURE 5 Different flow structures of three-phase C_s = 20% cap-bubble to slug flow transition of $J_g = 0.20$ m/s and $J_l = 1.50$ m/s.

the size of the cap bubble, resulting in Taylor's bubble. These Taylor bubbles are characterized by bullet-shaped bubbles with a diameter that occupies almost the entire cross-section of the pipe and a length bigger than one pipe diameter, promoting slugging and characterizing the slug flow pattern. Between these elongated bubbles and the pipe wall, an annular liquid film is observed, often referred to as a falling liquid film in situations that present downward movement. This film subsequently permeates the following liquid slug, creating a blending region saturated with tiny gas bubbles.[52,53] The liquid slugs that separate Taylor bubbles occupy all the pipe cross-sections and contain numerous dispersed small bubbles, with a similar geometrical distribution of the bubble or dispersed bubble flow patterns.

In the three-phase flow with 5%, it was observed that the majority of the solids were transported in the slug liquid. Additionally, particles were visualized in the liquid film, as shown in Figure 7. At this solid concentration, we noticed small oscillations in the gas–liquid interphase of the elongated bubble body. The oscillations are related to the impact of particles on the elongated bubbles. Rosas et al.[33] also visualized a similar behaviour for a horizontal pipe. The appearance of a wavy interface at the elongated bubble may also be related to the presence of particles in the annular liquid film, which may modify the flow in this region.

The increase to 10% and further to 20% of solid concentration showed similar effects to those previously described for the transition from cap bubble to slug pattern in elongated bubbles, as shown in Figures 8 and 9. With the increase in solid concentration, the amount of particles transported by the liquid film naturally increases. Consequently, the oscillation at the interface of the elongated bubble intensifies, and divergences in the shape of the gas–slurry bubble compared to the gas–liquid bubble become more visible. It was observed that the major part of solid transport occurs close to the nose of the elongated bubble in the slug liquid, and the region close to the tail predominantly contains bubbles. This effect was more evident in flows with 20% of solid.

The churn flow pattern is observed with the increase in the gas flow rate, typically visualized at elevated gas superficial velocities, as can be seen in Figure 10 for the

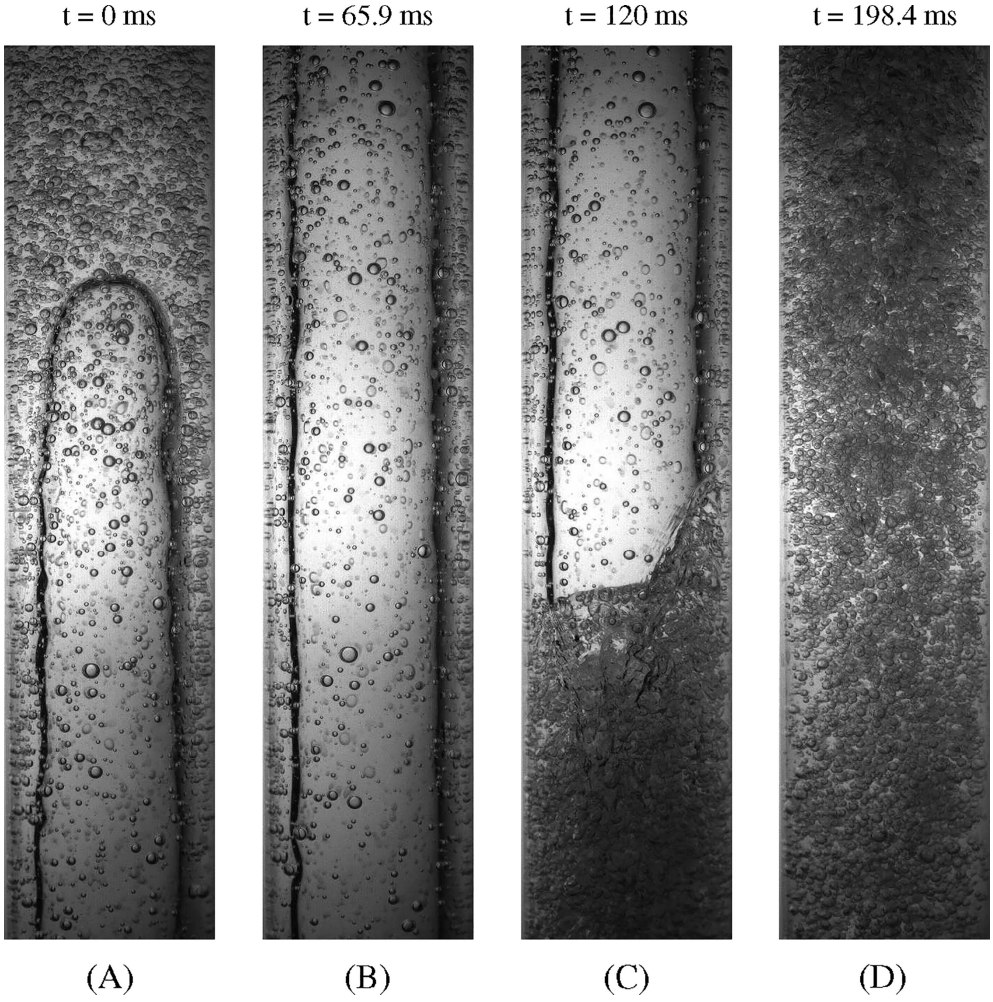

FIGURE 6 Two-phase slug flow pattern—$J_g = 0.50$ m/s and $J_l = 0.75$ m/s.

condition $J_g = 7.00\,\text{m/s}$ and $J_l = 0.75\,\text{m/s}$. Although it shares similarities with slug flow, churn flow appears more chaotic and disturbed. The churn elongated bubbles and slug liquid lack distinct boundaries between the two phases that are typically characteristic of slug flow, and there is a frequent presence of shorter and frothier liquid slug bridges with pipe diameters.[54] The nose of the elongated bubble rises and appears in the test section, with a high presence of dispersed small bubbles in the nose region, making the visualization of the interface format in this region challenging (see Figure 10A). In Figure 10B, the bubble diameter is significantly stable at this moment, with similar behaviour to the body of a high-speed slug flow pattern elongated bubble. The annular liquid surrounding the elongated bubble at this moment is moving upwards, in the same direction, as the gas bubble, but at a lower velocity. Subsequently, the annular liquid decelerates and starts to fall. Thus, the interface of the elongated bubbles increases the wavy shape, quickly scaling until the bubbles begin to break (see Figure 10C). The downward movement of the falling liquid creates waves large enough, resulting in short slug bridges that move downward. These bridges are sizeable enough to not be projected and cause the fragmentation of the long bubble (see Figure 10D). These short slug caps fall back with the previous movement until being pushed with high intensity by the next fragmented or elongated bubble, due to a considerably higher gas injection than the liquid. Consequently, the characteristic bullet-shaped Taylor bubbles are not visible, and the elongated bubbles have distortion, giving rise to churning phenomena.[50] These churn elongated bubbles are separated by a large slug of liquid with high air bubble dispersion, pushed by the next elongated gas churn unit (see Figure 10E). Although it is a well-known flow pattern, there is still a lack of consensus regarding the proper definition. It is distinguished by the rhythmic, oscillatory motion of the liquid phase with large waves and with liquid carried as drops, and being a gas-dominated flow.[55]

The presence of particles in the churn flow patterns demonstrated that elongated bubbles tend to be larger than in the two-phase flow churn. The same two-phase churn stages previously described are visualized with slurry flow with 5%, 10%, and 20% of solids concentration, in Figures 11–13, respectively. A similar effect of

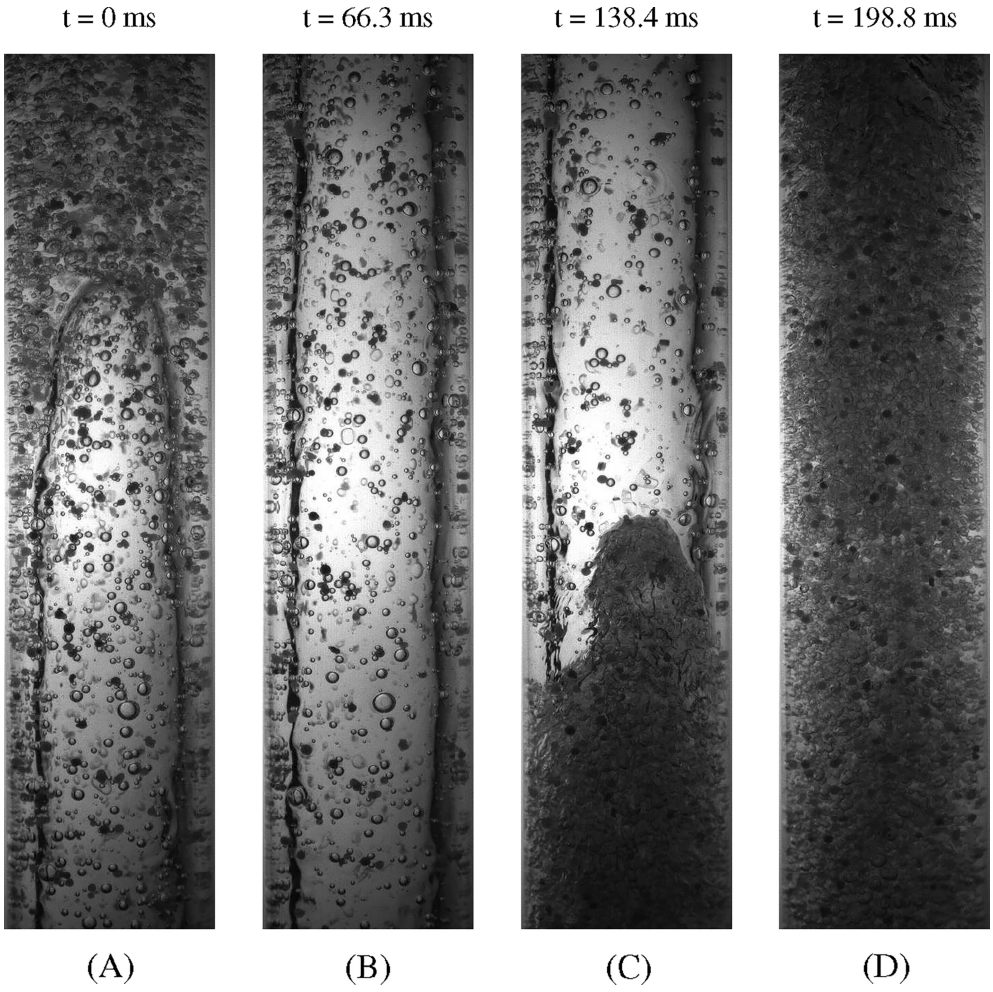

FIGURE 7 Three-phase 5% solid concentration slug flow pattern–$J_g = 0.50\,\text{m/s}$ and $J_l = 0.75\,\text{m/s}$.

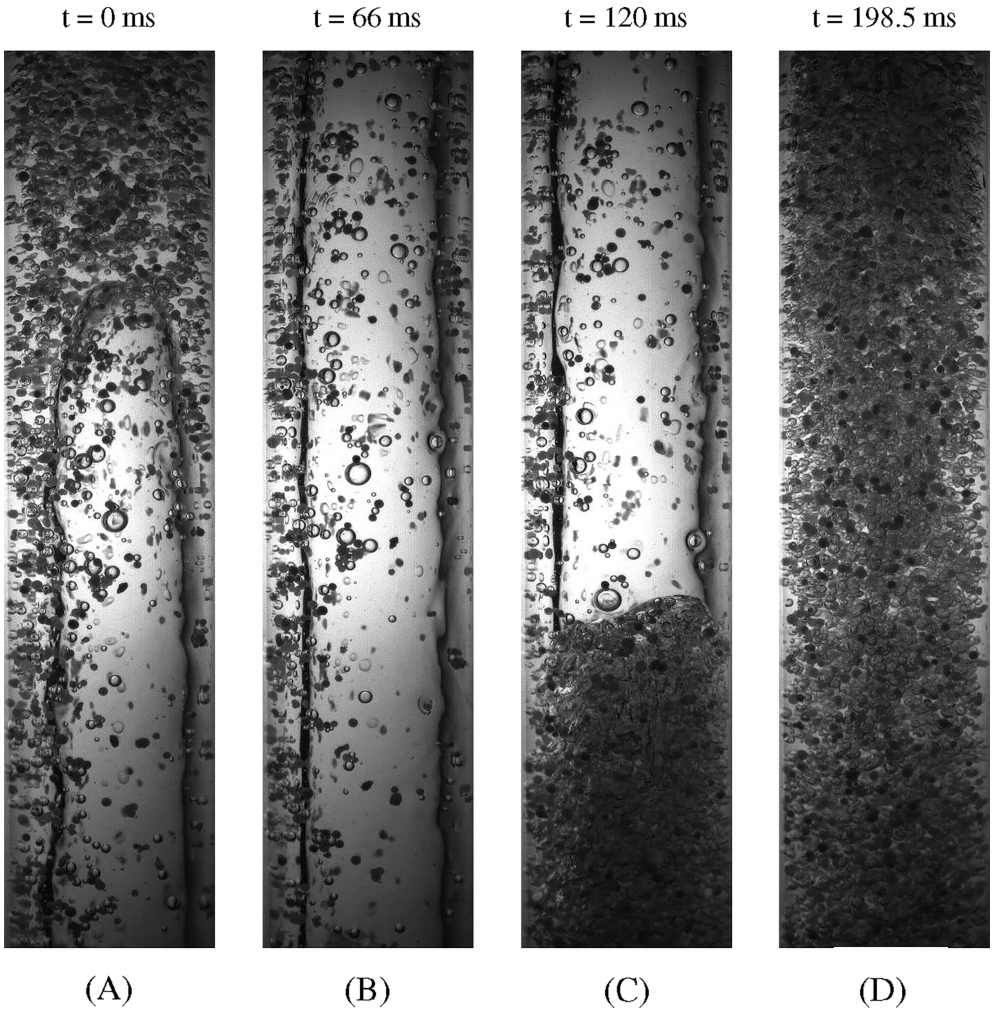

FIGURE 8 Three-phase 10% solid concentration slug flow pattern–$J_g = 0.50$ m/s and $J_l = 0.75$ m/s.

reducing the size and quantity of bubbles in the liquid slugs was observed in the churn flow pattern, which justifies the qualitative increase of the elongated bubbles. However, this effect is not as evident as the cap-bubble and slug flow patterns.

At relatively high liquid flow rates, the dispersed bubble flow pattern is predominant. At these high liquid velocities, the effect of bubble agglomeration and coalescence is overcome by large turbulence forces. The liquid phase becomes dominant, carrying the small gas bubbles, in a way that this flow pattern might be considered to exhibit a homogeneous no-slip behaviour, without any significant slippage between the phases well-mixed and with strong interaction[50] (see Figure 14). This flow pattern might exhibit significantly higher volumetric gas concentrations, with some reports indicating values up to 0.52–0.74.[9,56] In the dispersed bubble flow pattern, a reduction in dispersed bubbles was noted in proportion to the increase in particles. Thus, for 10% and 20% slurry flows, the majority of the gas phase was transported in clusters of bubbles. Therefore, analyzing this flow as a gas–liquid slurry, the presence of particles postpones the transition from any flow pattern to the dispersed bubble regime.

In summary, three main effects of the solid phase might be highlighted: first, a retardation or delay in the transition between flow patterns compared to gas–liquid flow test cases; second, a notable alteration in the shape of the gas–liquid interface or an additional variation in some interface characteristic; and third, a qualitatively visible reduction in the number of dispersed bubbles and a modification on the sizes of these bubbles, mainly observed in the dispersed bubble and slug flow pattern. This paper does not aim to discuss if the solid phase assumes or not different periodic and well-established geometrical distributions (patterns) with their characteristics. Although some observations showed this possibility, further study is required to evaluate these conditions.

Furthermore, since the solid particles are less dense than water, a considerable number of particles tend to be suspended in the flow and accumulate close to the nose of the elongated bubbles, or at the annular liquid film, and interacting with the high aerated tails of the elongated bubble, counteracting gravity. The intense interaction

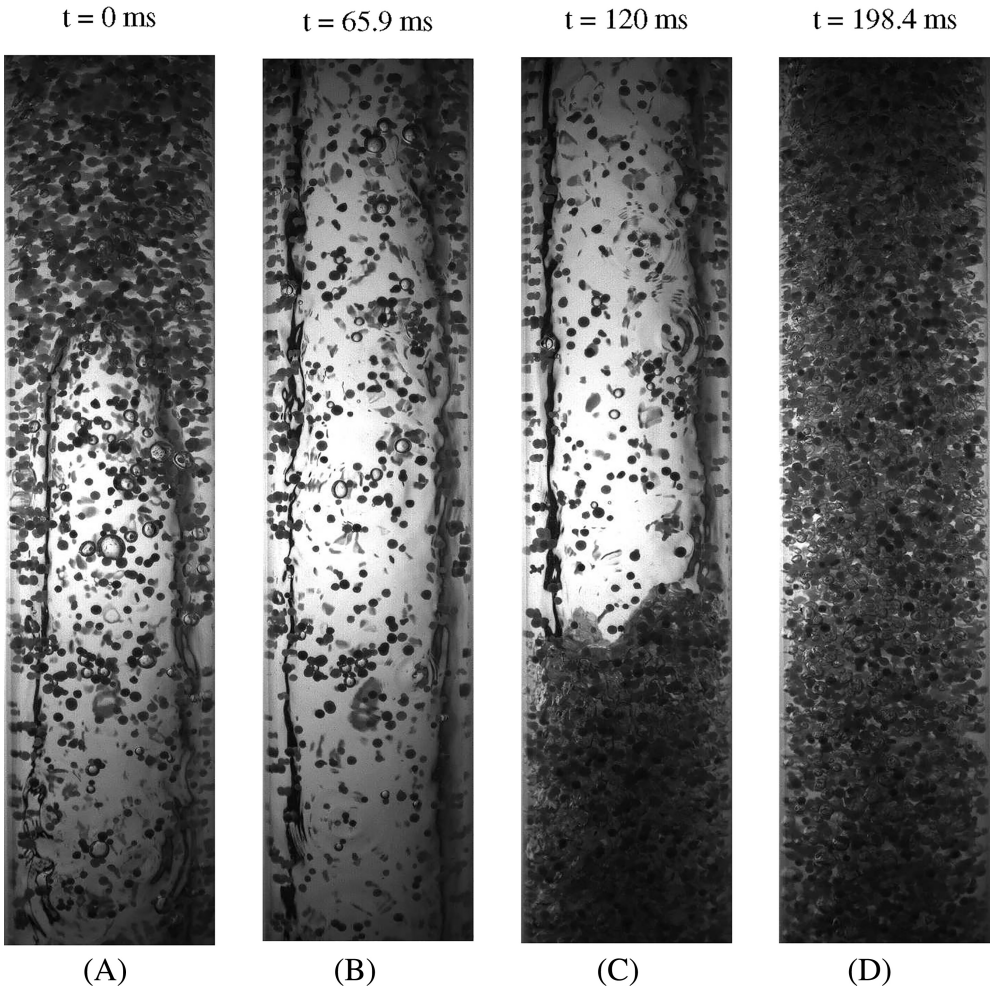

FIGURE 9 Three-phase 20% solid concentration slug flow pattern–$J_g = 0.50$ m/s and $J_l = 0.75$ m/s.

between the interface of the slug flow pattern and particles justifies the early transition from slug to churn. The buoyancy in the present experiments enhances the transportation of solid particles throughout the liquid phase.

3.3 | Flow pattern map

The flow pattern visualization described above provides the criteria to classify experimental measurements for the operating conditions indicated in Table 3. Therefore, the images of each test condition were analyzed to construct a flow regime map for different flow rates at each solid concentration. In total, 179 unique test cases were classified. Figure 15 presents the flow pattern map for the two-phase and three-phase flow for the three different solid concentrations.

The transitions between the patterns were compared with the transitional models proposed by Barnea[57] and McQuillan and Whalley.[56] The model of Barnea[57] is commonly used to predict the transition slug-to-churn flow pattern and from slug to dispersed bubble patterns.[10] This correlation was modified from the one proposed by Taitel et al.[9] and is defined as shown in Equation (6).

$$J_l = 6.14D^{0.43}\left(\frac{\sigma}{\rho_l}\right)^{0.54}\left(\frac{\rho_l}{\mu_l}\right)^{0.071}\left(\frac{g\left(\rho_l-\rho_g\right)}{\sigma}\right)^{0.45} - J_g \quad (6)$$

Additionally, the model proposed by McQuillan and Whalley[56] was used to predict the transition from cap-slug and slug to dispersed flow. This model is defined with the Equation (7).

$$J_l = \frac{6.8}{\rho_l^{0.444}}\left[g\sigma\left(\rho_l-\rho_g\right)\right]^{0.278}\left(\frac{D}{\mu_l}\right)^{0.112} \quad (7)$$

Both correlations adopted in the present study suggest a maximum gas holdup value at which the dispersed bubble flow pattern can occur. A maximum value of $H_g = 0.74$ was suggested by McQuillan and Whalley,[56] while Taitel et al.[9] and Barnea[57] models used a value of $H_g = 0.54$. Therefore, the transition from the churn flow pattern to dispersed bubbles can be

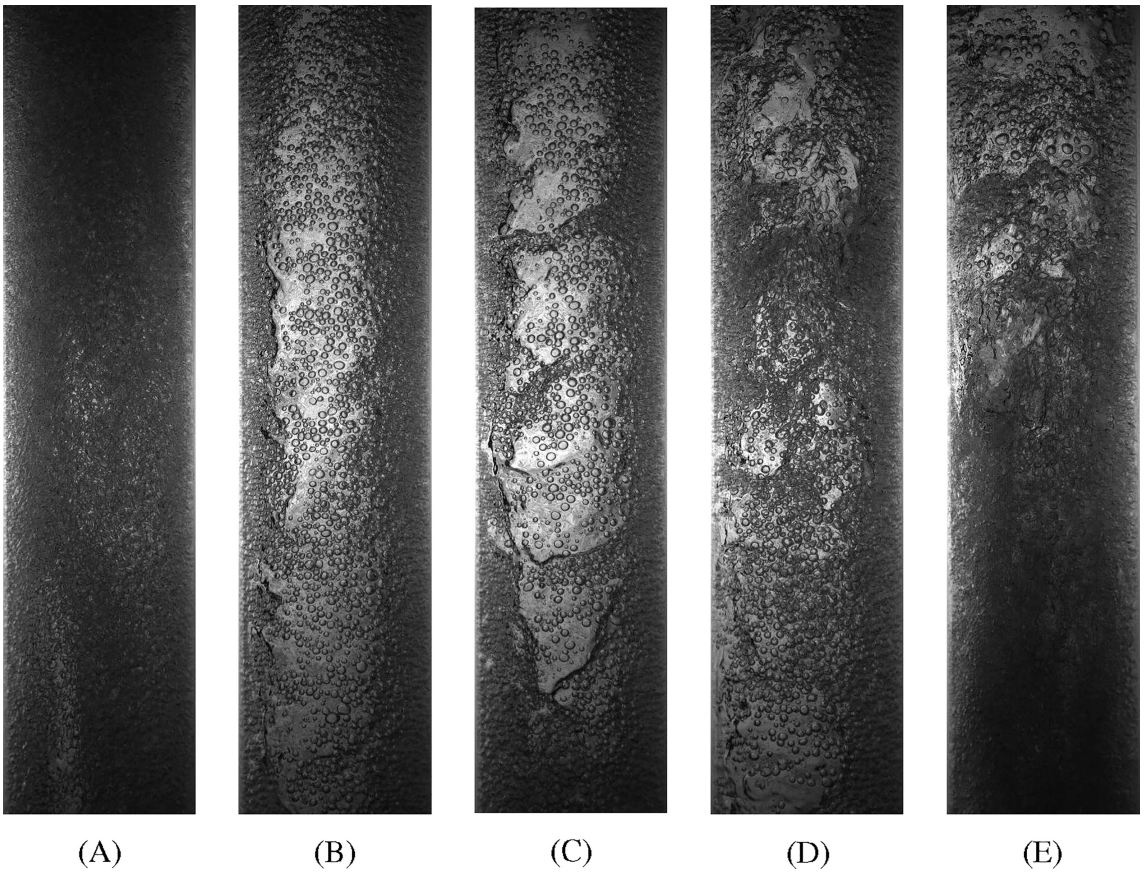

FIGURE 10 Images of different flow structures of two-phase churn flow pattern–$J_g = 7.00$ m/s—$J_l = 0.75$ m/s.

estimated using Equation (8) combined with these suggested values.

$$J_l = \left(\frac{1 - H_g}{H_g}\right) J_g \tag{8}$$

To apply these transition models to the gas–liquid–solid flow cases, the liquid and solid were treated as a single pseudo-slurry phase, with the calculated mixture density and viscosity. Based on the Equation (1) the density for 5%, 10%, and 20% of solids are 991.59, 984.98, and 971.76 kg/m^3, respectively. The slurry viscosities were calculated with the Equation (2), being 1.13×10^{-3}, 1.32×10^{-3}, and 2.11×10^{-3} Pa · s for 5%, 10%, and 20% of solids, respectively.

Figure 15 presents the comparison with and without the adjustment of slurry density and viscosity on the two transition correlations adopted. With the modification, a low impact on the predictions of transition models was obtained with the adjusting of slurry viscosity and density for the test cases with 5% and 10% of solid concentration. The influence of the slurry viscosity and density on the Barnea[57] and McQuillan and Whalley[56] models was more visible in the cases with 20% (see Figure 15D).

Table 4 presents the evaluation of these two flow pattern transition models for two- and three-phase flows. The successful prediction rate for each flow pattern is displayed based on the number of cases located inside the expected region. The unsuccessful predicted rate takes into account the number of visualized patterns outside the expected prediction region, divided by the total number of cases of the respective solid concentration. For H_s equal to 10% and 20%, the dispersed bubble pattern was not considered, as this flow regime was not visualized for these conditions.

It is observed that an increase in particle concentrations from $H_s = 0\%$ to $H_s = 5\%$ does not provide significant changes in the flow pattern classification, as shown in Figure 15B. When the solid concentration increases to $H_s = 10\%$, there is a reduction in the cap-slug area and an increase in the presence of the churn flow pattern for cases with average liquid superficial velocity and high gas superficial velocity, as seen in Figure 15C. Additionally, the presence of the dispersed bubble pattern for $J_l > 3$ m/s is no longer observed, and a transition regime was visible with characteristics between cap-dispersed bubbles. As the solid concentration increases to 20%, the churn flow pattern becomes visible for significantly lower gas

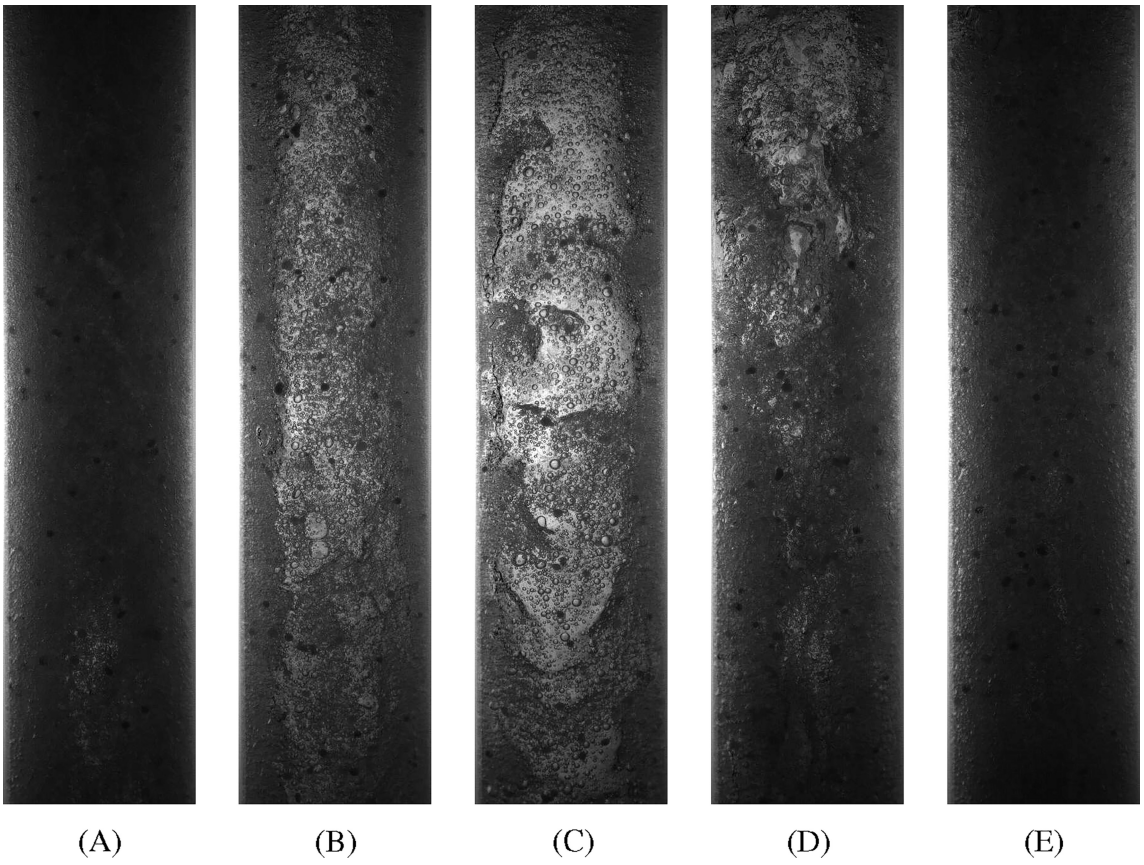

FIGURE 11 Images of different flow structures of three-phase 5% solid concentration churn flow pattern—$J_g = 7.00$ m/s—$J_l = 0.75$ m/s.

superficial velocities compared to the two-phase cases and the other solid concentrations, as shown in Figure 15D. The characteristics of the dispersed bubble pattern reduce even further and present a significant transformation.

It is noted that the transition from slug to churn flow occurs at lower gas superficial velocities with the increase of particles, as previously described in Section 3.2 (see Figure 15). Thus, these transitions to three-phase flow with 10% solid concentration have the most conforming points to the approach of Barnea.[57] However, the effectiveness of the model was slightly reduced with the increase in concentration to 20%. This is due to the effect of the transition from slug to churn appearing at lower gas-superficial velocities, and the churn flow pattern started to be visualized in regions where slug is dominant in cases of two-phase flow, especially at lower liquid superficial velocities.

Furthermore, the predicted transition from the two correlations with adapted viscosity and density indicated lower values of J_l for the transition from cap-slug, slug, or churn to a dispersed flow pattern. Nevertheless, an opposite trend was observed, as shown in Figure 15 and discussed in Section 3.2. Similarly, the Barnea[57] correlation with adapted viscosity and density predicted a reduction in the J_g for the transition between slug and churn flow patterns compared to the two-phase flow. However, these adjustments alone do not sufficiently improve flow pattern transition predictions. This might be related to multiple effects due to the presence of the solid being not considered. For instance, higher solid concentrations significantly increase the apparent viscosity and the particle–particle interaction.[58,59] Additionally, in a three-phase flow, the presence of suspended solids increases the bubble coalescence.[32]

The application of two-phase flow pattern transition models shows potential for predicting gas–liquid–solid systems, but as discussed, there are limitations. For instance, developing flow pattern correlations for three-phase flows requires further research on varying densities, concentrations, and shapes of the solid particles.

3.4 | Volumetric phase fraction

Figure 16 shows the experimental results for the liquid holdup (H_l) and slurry holdup (H_{sl}) measurements for two- and three-phase as a function of gas superficial velocity for three fixed liquid superficial velocities ($J_l = 0.75$, 1.50, and 2.00 m/s). The liquid holdup of the

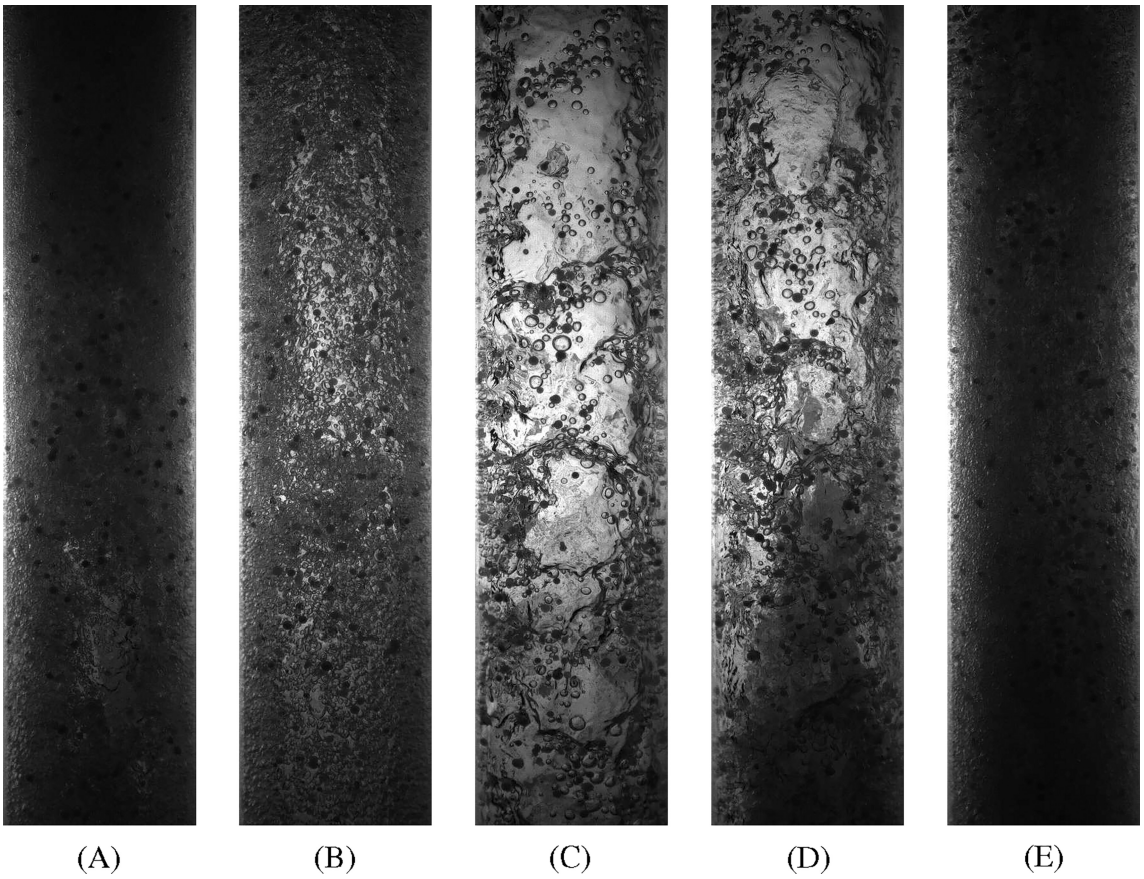

FIGURE 12 Images of different flow structures of three-phase 10% solid concentration churn flow pattern—$J_g = 7.00$ m/s—$J_l = 0.75$ m/s.

two-phase cases is also plotted to facilitate the comparison. Logically, H_{sl} has a bigger value regarding the liquid holdup for each respective case since it is composed of $H_l + H_s$.

Figure 16A, corresponding to the case of the lower liquid superficial velocity of $J_l = 0.75$ m/s, shows that an increase of J_g induces an asymptotic decrease in liquid holdup before reaching a relatively constant value of about 0.34 in the two-phase flow cases. It also appears that the decrease in the slope variation of the liquid holdup corresponds to the transition to churn flow, as was similarly observed by Bhagwat and Ghajar.[60] A similar behaviour of reduction of the holdup is also observed for three-phase flow at the three different solid concentrations investigated. Notably, the reduction of the liquid holdup variation slope is not related to the slug-to-churn flow transition for the case of 20% concentration. This flow transition occurs at lower gas superficial velocities in comparison to the other solid concentrations, as discussed in the previous subsection.

By comparing the results depicted in Figure 16A,C,E, we can observe that an increase in liquid superficial velocities results in an increase in liquid holdup. As expected, the reduction in liquid holdup (H_l) continues to be directly related to the increase in gas superficial velocity. We can also deduce that the increase of J_l shifts the critical value when H_l becomes constant to higher values of J_g. This may be due to the fact that the increase in the liquid superficial velocity from 0.75 to 1.50 m/s makes the liquid phase more significant in terms of the geometric distribution of the phases. This might be assumed as a hypothesis since for cases 1.50 m/s a slight drop in H_{sl} measurements is observed in the cap-slug and slug patterns, however, this effect is not visible for cases with $J_l = 2.00$ m/s. Comparing the different solid concentrations at fixed J_l and J_g, we can note that at low gas superficial velocities (mainly at $J_g = 0.2$ m/s) there is a reduction in H_l related to the volume occupied by the solid particles. This difference reduces with the increase in J_g. However, for some test cases with $J_l = 0.75$ m/s, the difference in H_l between the solid concentration cases becomes imperceptible, especially in the slug and churn patterns (see Figure 16A). This situation was different for cases with $J_l = 1.5$ and 2.0 m/s, where cases with 20% solid concentration present the lowest liquid holdup measurements, with some exceptions for high gas superficial velocities on the churn flow pattern (see Figure 16D,F). A similar situation was observed for cases with 10% solid concentration and for

THE CANADIAN JOURNAL OF CHEMICAL ENGINEERING

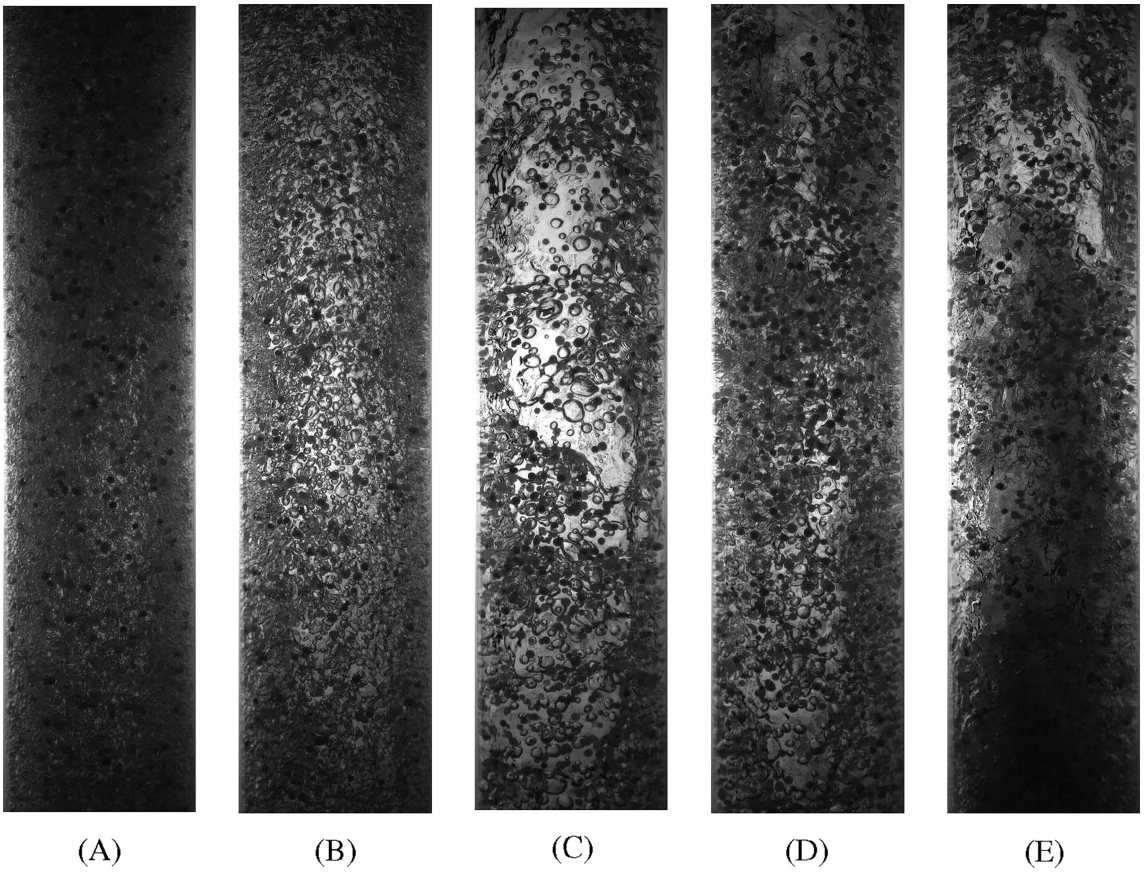

FIGURE 13 Images of different flow structures of three-phase 20% solid concentration churn flow pattern—$J_g = 7.00$ m/s—$J_l = 0.75$ m/s.

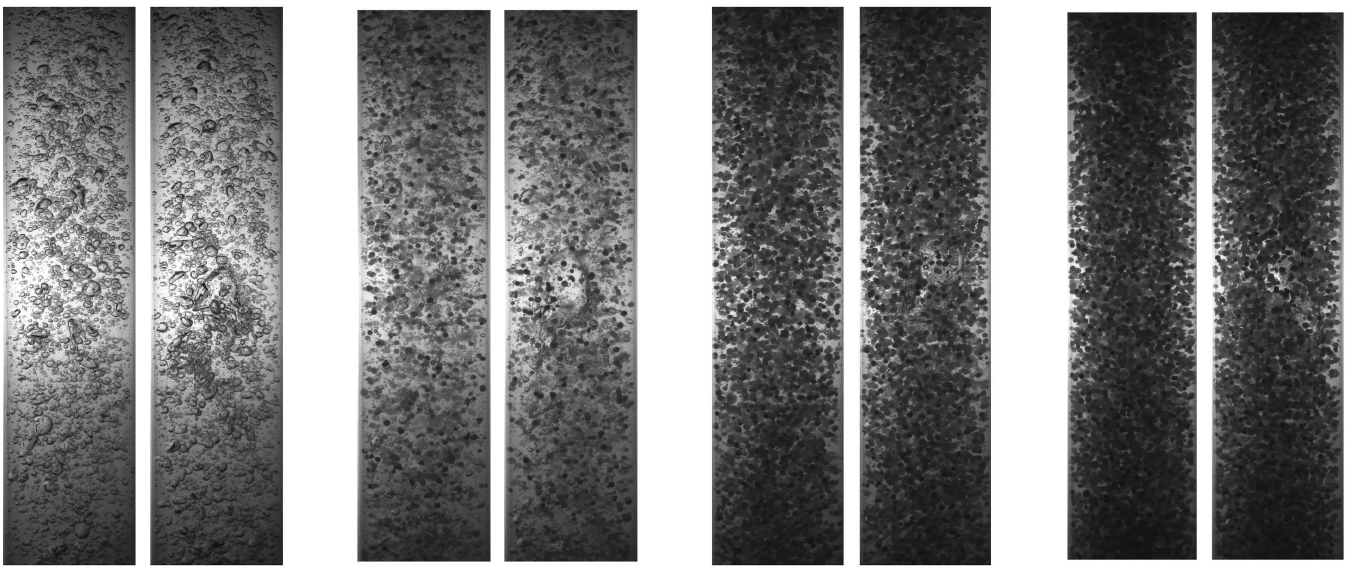

FIGURE 14 Comparison disperse bubble flow pattern with $J_g = 0.2$ m/s and $J_l = 3.00$ m/s over the solid concentrations.

the 5% cases. However, at this lower solid concentration, H_l measurements are significantly closer to those found in gas–liquid cases.

An important reduction of H_{sl} occurs from the cap-slug until the end of slug flow patterns. This tendency diminishes with the increase of J_l. Thus, H_{sl} presents the

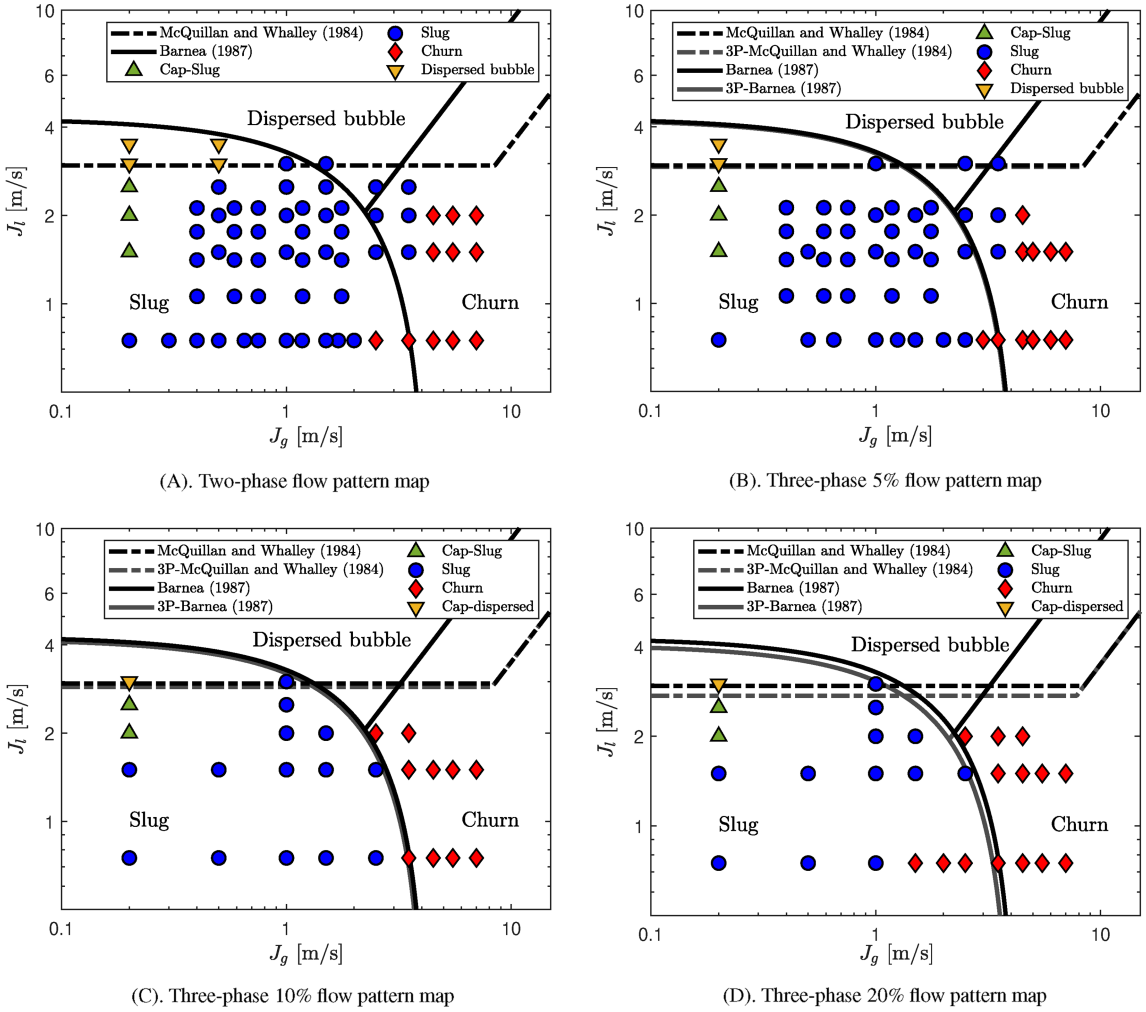

FIGURE 15 Flow regime map plotted against transition curves from models of Barnea[57] and McQuillan and Whalley.[56]

TABLE 4 Flow pattern prediction with Barnea[57] and McQuillan and Whalley[56] correlation for the two- and three-phase data.

		Two-phase	Three-phase		
		0%	5%	10%	20%
McQuillan and Whalley[56]					
	Dispersed bubble	100%	100%	-	-
	Slug	95.8%	92.5%	92.3%	96.5%
	Cap-slug	100%	100%	100%	100%
	Unsuccessful (%)	3.0%	5.3%	3.7%	3.3%
Barnea[57]					
	Slug	87.5%	92.9%	100%	100%
	Churn	81.8%	83.3%	90.0%	71.4%
	Dispersed bubble	0%	0%	-	-
	Unsuccessful (%)	12.1%	12.3%	3.7%	13.8%

same behaviour as observed for H_l. It is noted that the reduction in H_l with increasing solids concentration is not observed with the slurry holdup. There is a small predisposition of three-phase cases with 20%, in which most of the H_{sl} measurements are slightly higher than the other cases for the condition of $J_l = 0.75$ m/s,

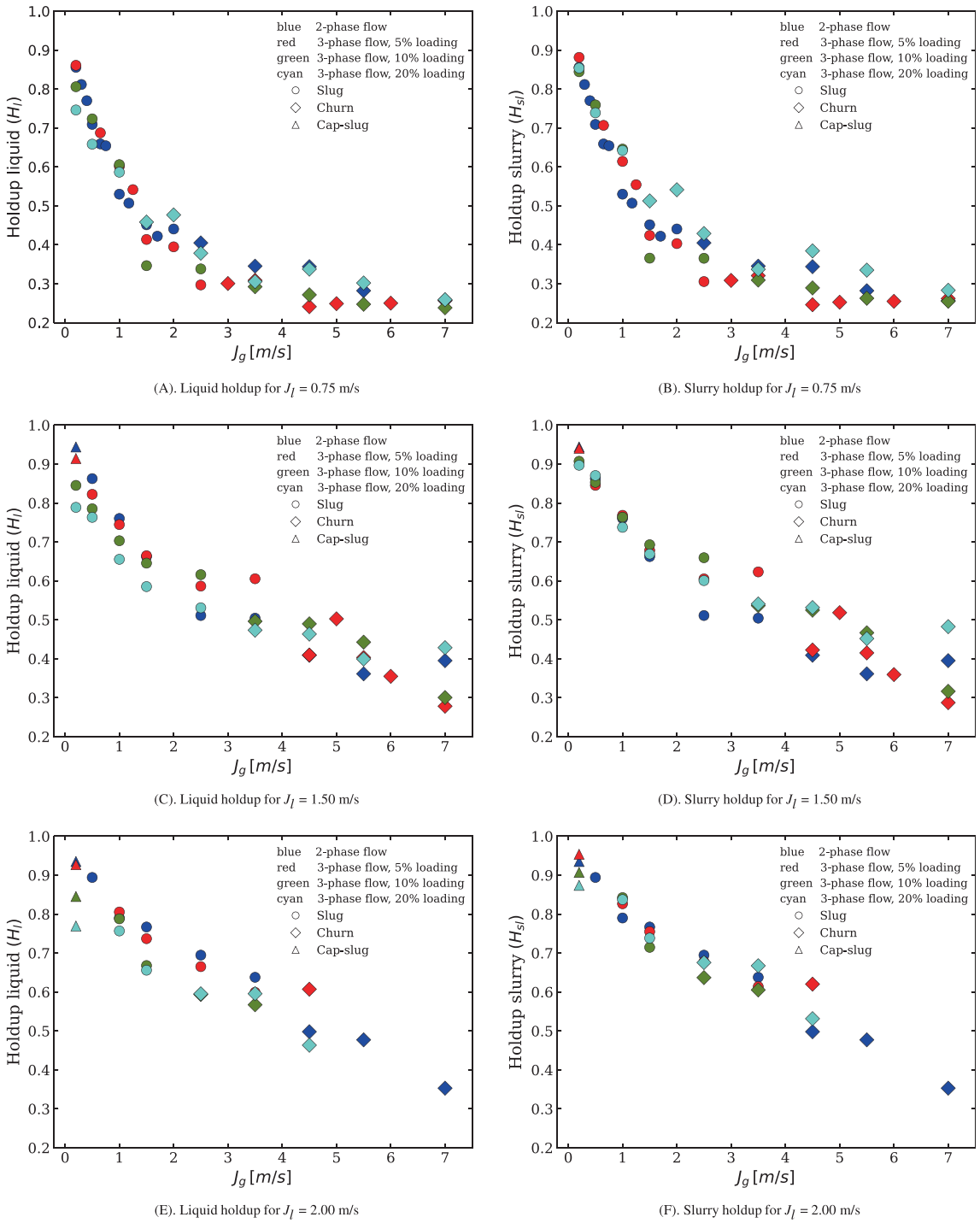

FIGURE 16 Liquid holdup and slurry holdup by different gas superficial velocity for fixed J_l.

Figure 16A. Although this situation was not visible for the other cases in which $J_l = 1.50$ and 2.00 m/s. Therefore, it can be verified that there is no impact on the average gas holdup for concentrations of up to 20% solids in the slurry liquid. This was also reported by Hatate et al.[39] in upward vertical flows with particles with a density of 2520 kg/m^3.

The predictions given by ten liquid holdup models are assessed with the measured database of this study using the statistical parameters APD, AAPD, and RMSPD, defined in Equations (3)–(5). The results of the assessement are summarized in Table 5. In order to calculate the slurry holdup (H_{sl}), the solid and liquid phases were considered as one pseudophase. To facilitate the use of two-phase correlation in the gas–liquid–solid flow, the

TABLE 5 Assessment of the liquid holdup correlation with the two- and three-phase experimental data.

	Two-phase			Three-phase 5%			Three-phase 10%			Three-phase 20%		
	APD	AAPD	RMSPD	APD	AAPD	RMSPD	APD	AAPD	RMSPD	APD	AAPD	RMSPD
Nicklin[18]	−4.52	6.83	8.89	−4.66	10.50	13.11	−5.20	10.68	13.56	−11.58	12.31	14.96
Chisholm[19]	−3.29	15.46	17.58	0.55	19.67	25.49	2.93	21.09	26.36	−3.72	13.18	15.66
Rouhani and Axelsson[20]	−4.56	6.84	8.90	−4.71	10.48	13.09	−5.28	10.62	13.55	−11.64	12.36	15.02
Bonnecaze et al.[21]	−4.52	6.84	8.89	−4.66	10.50	13.11	−5.21	10.68	13.56	−11.58	12.31	14.96
Beggs and Brill[22]	−8.09	9.69	12.25	−7.82	13.11	15.69	−8.33	13.87	16.43	−14.19	14.79	17.89
Huq and Loth[23]	−2.80	7.01	8.17	−2.11	11.05	13.70	−2.11	11.42	13.62	−8.69	9.65	11.42
Woldesemayat and Ghajar[16]	−8.71	11.43	13.32	−7.48	15.59	17.91	−6.75	16.25	17.90	−13.20	13.93	16.18
Armand—Massena	−7.69	8.67	10.71	−8.12	11.39	13.79	−8.85	10.92	14.37	−14.93	15.49	17.97
Kanizawa and Ribatski[24]	−75.81	75.81	76.19	−79.51	79.51	79.84	−82.70	82.70	83.06	−90.58	90.58	90.73
Almabrok et al.[25]	−19.31	19.71	23.94	−22.20	22.80	26.61	−24.81	24.92	29.76	−29.27	29.57	34.67
AlSaif and Al-Sarkhi[26]	−8.47	11.10	14.95	−10.39	12.96	17.15	−12.53	15.65	19.90	−17.89	18.79	23.70

Abbreviations: AAPD, average absolute percentage difference; APD, average percentage difference; RMSPD, root mean square percentage difference.

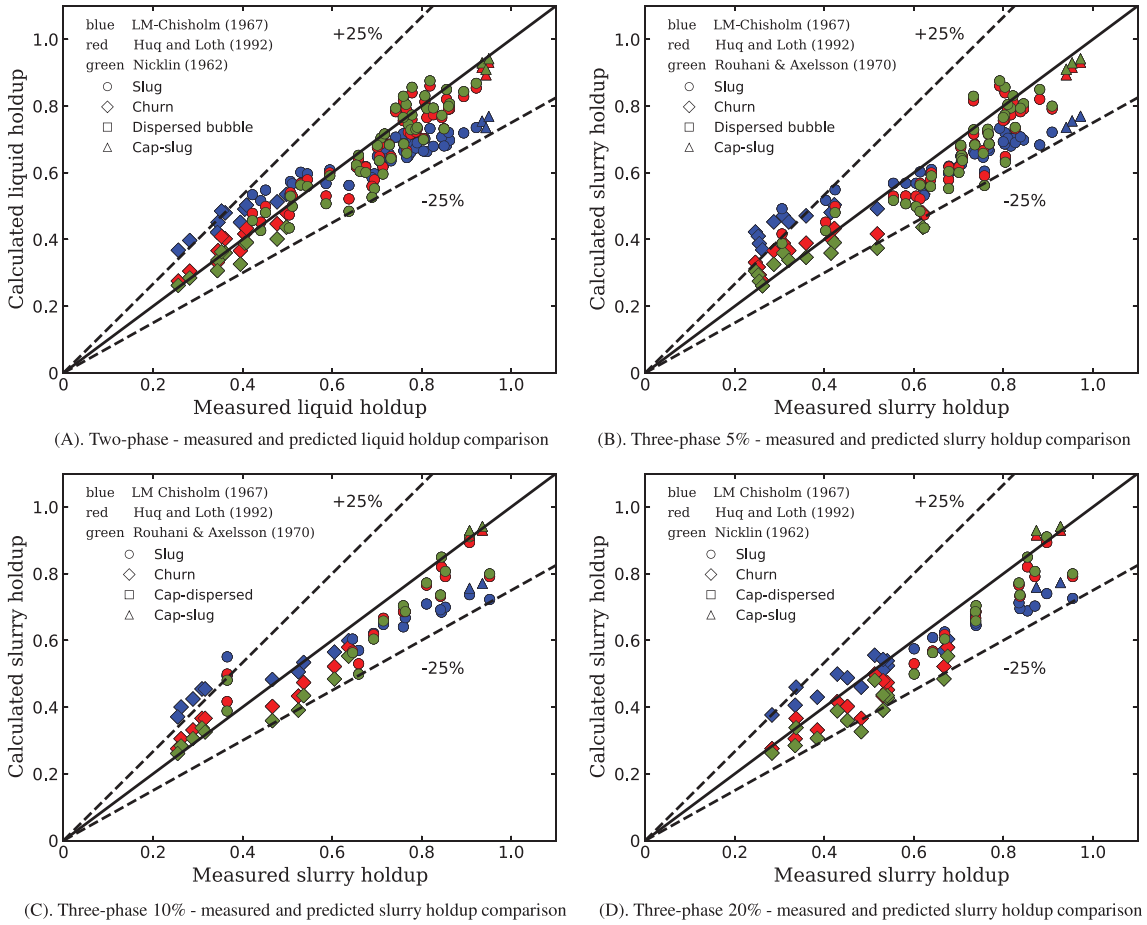

(A). Two-phase - measured and predicted liquid holdup comparison

(B). Three-phase 5% - measured and predicted slurry holdup comparison

(C). Three-phase 10% - measured and predicted slurry holdup comparison

(D). Three-phase 20% - measured and predicted slurry holdup comparison

FIGURE 17 Assessment of the liquid holdup correlation with the two- and three-phase experimental data for the general experimental data and visualized flow patterns.[18–20,23]

density and viscosity of this slurry phase were calculated with the Equations (1) and (2).

The same models with higher statistical values for two-phase flow also showed less favourable results for the three-phase cases with 5%, 10%, and 20% solid concentrations. However, most of the statistical parameters show a tendency to increase with the rise in the solid concentration. For two-phase flow cases,

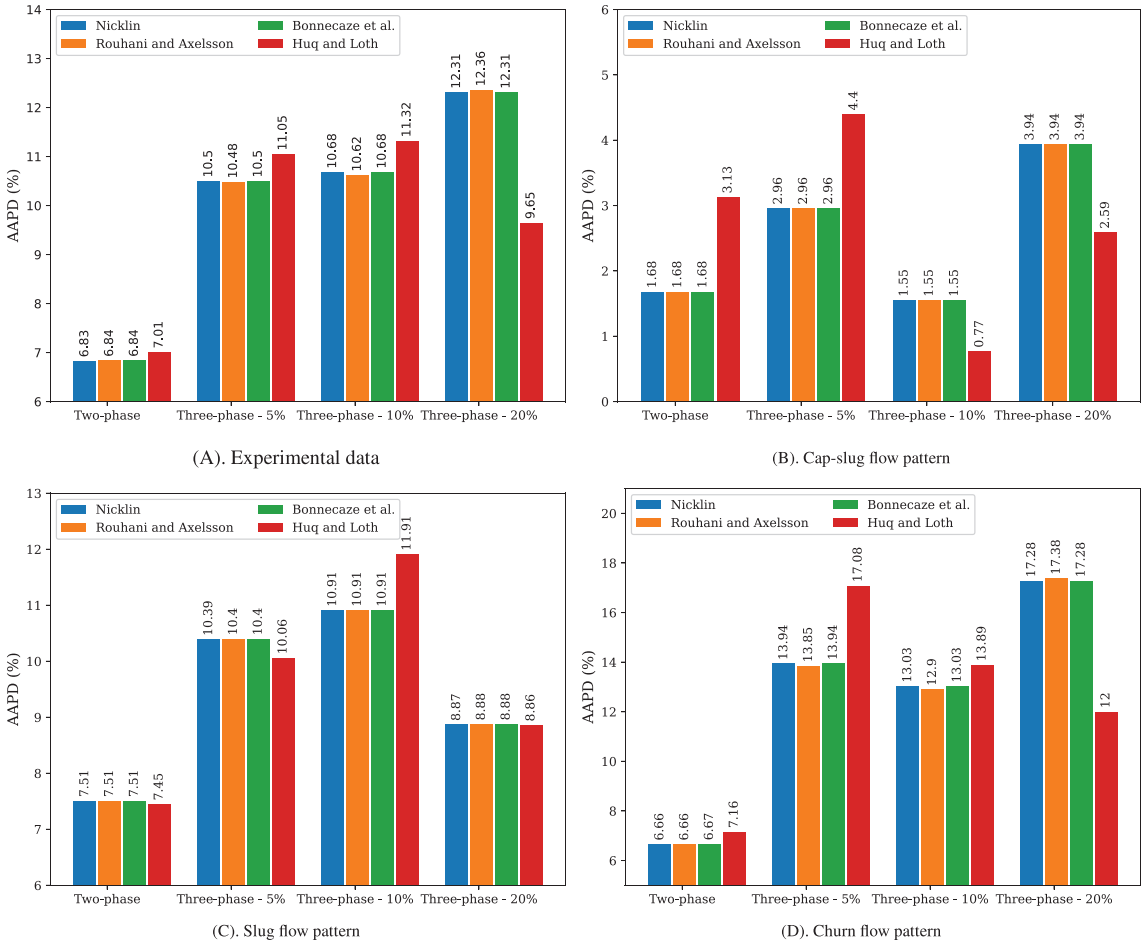

FIGURE 18 Comparison between measured H_l and H_{sl} with the prediction of the volumetric fraction correlations.[18,20,21,23]

the model proposed by Huq and Loth[23] achieved the best results with values of −2.8% and 8.17% by APD and RMSPD, respectively. The best result for AAPD for two-phase flow cases was obtained with the model proposed by Nicklin,[18] which had a positive RMSPD value of 8.89%. The models proposed by Rouhani and Axelsson[20] and Bonnecaze et al.[21] also yielded positive results, with RMSPD values of 8.9% and 8.89%, respectively.

Figure 17 compares the measured values of H_l for two-phase flow or H_{ls} for three-phase flow for the three solid concentrations with the correlations that achieved the satisfactory evaluation of the statistical parameters. Besides, for each solid concentration and the two-phase flow, the model with the best performance varies. The model of Huq and Loth[23] is found to be the most appropriate model for predicting the (H_{sl}) for the cases with $H_s = 20\%$, and presents good performance for the two-phase data. However, this correlation appears to lose performance for the cases with $H_s = 5\%$ and 10%. For the cases of $H_s = 5\%$ and 10%, the models of Chisholm[19] obtained lower APD values but did not perform well considering AAPD and RMSPD. The Rouhani and Axelsson[20] correlation gives the best predictions considering the AAPD and RMSPD values for the cases with $H_s = 5\%$ and 10%. For the case of $H_s = 20\%$, the model of Nicklin[18] gives the best results after the model of Huq and Loth.[23] It is noted that for cases with a 5% slurry concentration, the results of APD are similar to those obtained for two-phase flow cases, with some models showing better APD results for $H_l = 5\%$ than for two-phase flow, such as those obtained by the models of Huq and Loth[23] and Woldesemayat and Ghajar.[16] An APD value of 0.55% was obtained using the model proposed by Chisholm.[19] However, this same model had an AAPD value of 19.67%.

Figure 18 compares the AAPD values for the best-performing correlations in the two-phase experimental cases and the three different solids concentrations in the three-phase cases. In general, the four best correlations, those proposed by Nicklin,[18] Rouhani and Axelsson,[20] Bonnecaze et al.,[21] and Huq and Loth,[23] show similar trends for both the overall data and the data from different flow patterns. A reduction in the accuracy of

predictions is observed with increasing solids concentration when evaluating the data as a whole (see Figure 18A). This same trend is also observed for the churn flow pattern (see Figure 18D). However, for the slug flow pattern, cases with 20% solids concentration show lower AAPD values compared to the other two three-phase flow configurations (see Figure 18C). For the cap-slug flow pattern, the cases with 10% solids concentration show lower AAPD values than the two-phase cases (see Figure 18B). It is important to note that cap-slug flow pattern has few data points in this study and this may affect this tendency.

The models proposed by Nicklin,[18] Rouhani and Axelsson,[20] and Bonnecaze et al.[21] show very similar performance in terms of AAPD. As a result, the best correlation varies depending on the flow pattern. Nicklin's correlation either achieved the best results or results close to the best, maintaining consistency across conditions (see Figure 18). Additionally, it is a simple correlation based on J_l and J_g. For solid concentrations of 5% and 10%, the model proposed by Rouhani and Axelsson stands out with satisfactory results for both AAPD and RMSPD for the different flow patterns. For cases with higher solids concentrations, the Huq and Loth[23] model stands out. This correlation provides the best results for cases with $H_{ls} = 20\%$ solids concentration when evaluating the overall data and for churn flow patterns (see Figure 18A,D). Table A2 shows the assessment of correlations in terms of APD, AAPD, and RMSPD for the two- and three-phase flow cases for the different flow patterns visualized in this study.

Through this method, the volumetric fraction correlation from Nicklin[18] might be recommended for general use in similar cases of two- and three-phase flows with particles less dense than water for the solid concentrations from 0% up to 20% on the liquid phase. This recommendation is due to its satisfactory performance across the three statistical parameters (APD, AAPD, and RMSD). In addition, this correlation presented a lower variance for the three different solid concentrations. Additionally, for cases with higher solid concentration, the correlation proposed by Huq and Loth[23] is appropriate, as it produced better results for cases with $H_{ls} = 20\%$. Furthermore, this study shows that the liquid holdup model developed for two-phase flow can be used for predicting slurry holdup in the case of three-phase flow with relatively good accuracy.

4 | CONCLUSIONS

The present experimental study aimed to better understand the vertical upward gas–liquid–solid three-phase flow using polypropylene particles, of sizes ranging between 1 and 3 mm, less dense than the liquid phase similar to gas hydrates. The effects of concentrated slurries with polypropylene particles on two-phase flow structures, flow patterns, and volumetric phase fractions have been analyzed. Common and well-known models and correlations for volumetric fractions were compared with the two-phase data, as well as the properties adapted and used to compare with the experimental three-phase data at three different solid concentrations.

Through flow visualization, it is found that higher solid concentrations in the slurry flow induce bigger deformations on the shape and interface of the slug flow pattern and an elongated bubble. Higher interfacial shear causes instabilities at the interface of gas and liquid, which sharpen the nose and shorten the elongated bubble. Furthermore, the transition from slug to churn flow pattern occurs at lower superficial velocity, and to achieve the dispersed bubble flow pattern, it requires higher liquid superficial velocities. The impacts created on the interface of the flow patterns, in the free bubbles on the liquid slugs and on the dispersed bubble pattern, do not significantly affect the gas holdup.

While investigating the gas holdup, it was found that the two-phase volumetric fraction correlation can be employed to calculate the gas volumetric fraction or the slurry volumetric fraction using a simple adjustment to the slurry viscosity and slurry density. Ten different two-phase flow liquid holdup models are assessed with the measured two- and three-phase database of this study using the statistical parameters APD, AAPD, and RMSPD. Among the assessed correlations, the model proposed by Nicklin[18] demonstrated satisfactory performance across all the measured conditions. This correlation might be employed under similar conditions for two- and three-phase flows with solid particles less dense than water. Additionally, for cases with high solid concentrations ($H_{ls} \geq 20\%$), the model by Huq and Loth[23] is suggested.

NOMENCLATURE

H	holdup/volumetric fraction (−)
K	flow parameter (−)
J	superficial velocity (ms^{-1})
g	gravitational acceleration (m/s^2)
D	pipe diameter (m)
X	Lockhart–Martinelli parameter (−)
x	mass quality (−)
C_0	velocity distribution coefficient (−)
U	velocity (ms^{-1})
G	total mass flux ($Kgm^{-2}s^{-1}$)
C	inclination correction factor (−)

P pressure (Pa)
We Weber number (−)
u_{gu} flow parameter (−)
d diameter

Greek letters

α void fraction (−)
ρ density (kg/m^3)
σ surface tension (Nm^{-1})
θ inclination angle (rad)
μ dynamic viscosity (Pa · s)

Subscripts

l liquid phase
H no-slip or homogeneous
k liquid or slurry phase
g gas phase
GM drift
atm atmospheric
sys system
m mixture
s solid phase
sl slurry phase

AUTHOR CONTRIBUTIONS

Ronaldo Luís Höhn: Conceptualization; methodology; investigation; validation; software; visualization; writing – original draft. **Abderraouf Arabi:** Conceptualization; validation; writing – original draft; software; visualization. **Sylvana Verónica Varela Ballesta:** Writing – review and editing. **Paolo Juan Sassi:** Writing – review and editing. **Jordi Pallarès:** Writing – review and editing; funding acquisition. **Youssef Stiriba:** Conceptualization; writing – original draft; software; visualization; funding acquisition; supervision.

ACKNOWLEDGEMENTS

This work was supported through the projects PID2020-113303GB-C21 and PID2023-146648NB-C21 funded by Ministerio de Ciencia e Innovación (MCIN) and Agencia Estatal de Investigación (AEI) and by project 2021SGR00732 from the Departament de Recerca i Universitats de la Generalitat de Catalunya as well as from the European Union's Horizon 2020 research and innovation programme under the Marie Skłodowska-Curie grant agreement Nos. 713679 and 945413, through the Martí Franquès COFUND Doctoral Programme. AA has received funding from the postdoctoral fellowships programme Beatriu de Pinós (2021 BP 00052), funded by the Secretary of Universities and Research (Government of Catalonia) and by the Horizon 2020 Programme of Research and Innovation of the European Union under the Marie Skłodowska-Curie grant agreement No. 801370.

PEER REVIEW

The peer review history for this article is available at https://www.webofscience.com/api/gateway/wos/peer-review/10.1002/cjce.25663.

DATA AVAILABILITY STATEMENT

The data that support the findings of this study are available from the corresponding author upon reasonable request.

ORCID

Abderraouf Arabi https://orcid.org/0000-0002-3581-5416
Youssef Stiriba https://orcid.org/0000-0002-0272-7807

REFERENCES

[1] O. T. Fajemidupe, A. M. Aliyu, Y. D. Baba, A. Archibong-Eso, H. Yeung, *Chem. Eng. Res. Des.* **2019**, *143*, 114.
[2] S. G. Holagh, W. H. Ahmed, *Int. J. Heat Mass Transfer* **2024**, *225*, 125422.
[3] J. G. Moguel-Castañeda, C. E. Rocha-Lara, C. E. Ramirez-Castelan, G. Soto-Cortes, E. Hernandez-Martinez, H. Puebla, *Can. J. Chem. Eng.* **2021**, *99*, 874.
[4] A. Arabi, R. L. Höhn, J. Pallares, Y. Stiriba, *Can. J. Chem. Eng.* **2024**, *103*, 2880.
[5] M. Abdulkadir, D. G. Jatto, L. A. Abdulkareem, D. Zhao, *Chem. Eng. Res. Des.* **2020**, *159*, 262.
[6] W. Chen, G. Huang, S. Li, F. Yang, Y. Hu, J. Yin, D. Wang, *Int. J. Heat Mass Transfer* **2024**, *219*, 124887.
[7] M. A. Tarahomi, M. Emamzadeh, M. Ameri, *Chem. Eng. Res. Des.* **2023**, *200*, 592.
[8] G. Soto-Cortes, E. Pereyra, C. Sarica, *Can. J. Chem. Eng.* **2025**, *103*, 442.
[9] Y. Taitel, D. Barnea, A. E. Dukler, *AIChE J.* **1980**, *26*, 345.
[10] B. Wu, M. Firouzi, M. Travis, T. E. Rufford, C. Leonardi, B. Towler, *Chem. Eng. J.* **2017**, *326*, 350.
[11] Z. Zhang, Z. Wang, H. Liu, Y. Gao, H. Li, B. Sun, *Int. J. Heat Mass Transfer* **2019**, *138*, 1346.
[12] P. Mondal, S. K. Lahiri, K. C. Ghanta, *Can. J. Chem. Eng.* **2024**, *102*, 4416.
[13] A. Arabi, F. Saidj, A. Al-Sarkhi, A. Azzi, *SPE J.* **2022**, *27*, 1577.
[14] M. Zhang, L. Pan, P. Ju, X. Yang, M. Ishii, *Int. J. Heat Mass Transfer* **2017**, *108*, 1579.
[15] M. S. Shadloo, A. Rahmat, A. Karimipour, S. Wongwises, *J. Energy Resour. Technol.* **2020**, *142*, 11.
[16] M. A. Woldesemayat, A. J. Ghajar, *Int. J. Multiphase Flow* **2007**, *33*, 347.
[17] L. Márquez-Torres, J. Ochoa-Pineda, P. Pico, J. P. Valdés, D. Becerra, A. Pinilla, E. Pereyra, N. Ratkovich, *SN Appl. Sci.* **2020**, *2*, 10.
[18] D. J. Nicklin, *Chem. Eng. Sci.* **1962**, *17*, 693.
[19] D. Chisholm, *Int. J. Heat Mass Transfer* **1967**, *10*, 1767.
[20] S. Z. Rouhani, E. Axelsson, *Int. J. Heat Mass Transfer* **1970**, *13*, 383.
[21] R. H. Bonnecaze, W. Erskine, E. J. Greskovich, *AIChE J.* **1971**, *17*, 1109.
[22] D. H. Beggs, J. P. Brill, *J. Pet. Technol.* **1973**, *25*, 607.

[23] R. Huq, J. L. Loth, *J. Thermophys. Heat Transfer* **1992**, *6*, 139.
[24] F. T. Kanizawa, G. Ribatski, *J. Braz. Soc. Mech. Sci. Eng.* **2015**, *38*, 209.
[25] A. A. Almabrok, A. M. Aliyu, Y. D. Baba, L. Lao, H. Yeung, *Heat Mass Transfer* **2017**, *54*, 209.
[26] A. AlSaif, A. Al-Sarkhi, *Results Eng.* **2024**, *21*, 101818.
[27] H. Fujimoto, T. Nagatani, H. Takuda, *Int. J. Multiphase Flow* **2005**, *31*, 1116.
[28] D. Zhang, S. Liu, J. Zhang, L. Hou, J. Xu, *ACS Omega* **2020**, *5*, 31262.
[29] J. Wang, Q. Zhang, R. Jin, L. Zhang, Y. Meng, H. Yao, L. Yang, J. Zhao, Y. Song, *J. Cleaner Prod.* **2023**, *430*, 139632.
[30] G. S. Patel, A. K. Jana, *Can. J. Chem. Eng.* **2025**, *103*, 1433.
[31] S. Hosokawa, H. Shakutsui, A. Tomiyama, *Multiphase Sci. Technol.* **2019**, *31*, 175.
[32] R. S. Douek, G. F. Hewitt, A. G. Livingston, *Chem. Eng. Sci.* **1997**, *52*, 4357.
[33] L. M. M. Rosas, C. L. Bassani, R. F. Alves, F. A. Schneider, M. A. M. Neto, R. E. M. Morales, A. K. Sum, *AIChE J.* **2018**, *64*, 2864.
[34] P. Sassi, Y. Stiriba, J. Lobera, V. Palero, J. Pallarès, *Flow, Turbul. Combust.* **2020**, *105*, 1035.
[35] P. Sassi, G. Fernández, Y. Stiriba, J. Pallarès, *Int. J. Multiphase Flow* **2022**, *149*, 103985.
[36] M. A. Rahman, K. F. Adane, R. S. Sanders, *Can. J. Chem. Eng.* **2013**, *91*, 1372.
[37] R. L. Miller, M. B. Cain, *Chem. Eng. Commun.* **1986**, *43*, 147.
[38] D. G. Thomas, *J. Colloid Sci.* **1965**, *20*, 267.
[39] Y. Hatate, H. Nomura, T. Fujita, S. Tajiri, N. Hidaka, A. Ikari, *J. Chem. Eng. Jpn.* **1986**, *19*, 56.
[40] T. Sakaguchi, H. Shakutsui, A. Tomiyama, H. Minagawa, H. Takahashi, *JSME Int. J., Ser. B* **1993**, *36*, 412.
[41] T. Sakaguchi, H. Minagawa, A. Tomiyama, H. Shakutsui, *Exp. Therm. Fluid Sci.* **1993**, *7*, 49.
[42] T. Yoshinaga, Y. Sato, *Int. J. Multiphase Flow* **1996**, *22*, 223.
[43] N. Hatta, M. Omodaka, F. Nakajima, T. Takatsu, H. Fujimoto, H. Takuda, *J. Fluids Eng.* **1999**, *121*, 330.
[44] F. F. Erian, L. F. Pease, *Int. J. Multiphase Flow* **2007**, *33*, 498.
[45] S. Z. Kassab, H. A. Kandil, H. A. Warda, W. H. Ahmed, *Chem. Eng. J.* **2007**, *131*, 273.
[46] S. Takano, S. Masanobu, S. Kanada, M. Ono, *Ocean Eng.* **2023**, *275*, 114121.
[47] S. Cavalli, R. F. Alaves, C. L. Bassani, M. A. M. Neto, A. K. Sum, R. E. M. Morales, *Chem. Eng. Sci.* **2024**, *300*, 120596.
[48] P. Sassi, J. Pallarès, Y. Stiriba, *Experimental and Computational Multiphase Flow* **2019**, *2*, 41.
[49] R. L. Höhn, A. Arabi, S. V. V. Ballesta, P. J. Sassi, J. Pallarès, Y. Stiriba, *Chem. Eng. Res. Des.* **2025**, *214*, 234.
[50] O. Shoham, *Mechanistic Modeling of Gas-Liquid Two-Phase Flow in Pipes*, Society of Petroleum Engineers, Richardson, TX **2006**.
[51] M. Abdulkadir, B. Ugwoke, L. A. Abdulkareem, D. Zhao, V. Hernandez-Perez, *Exp. Therm. Fluid Sci.* **2021**, *124*, 110349.
[52] L. Cheng, G. Ribatski, J. R. Thome, *Appl. Mech. Rev.* **2008**, *61*, 5.
[53] T. Wang, M. Gui, T. Zhang, Q. Bi, J. Zhao, Z. Liu, *Chem. Eng. Sci.* **2021**, *246*, 116895.
[54] S. Sharaf, G. P. van der Meulen, E. O. Agunlejika, B. J. Azzopardi, *Int. J. Multiphase Flow* **2016**, *78*, 88.
[55] Q. Y. Yang, N. D. Jin, L. S. Zhai, D. Y. Wang, F. Wang, *Exp. Therm. Fluid Sci.* **2019**, *107*, 16.
[56] K. W. McQuillan, P. B. Whalley, *Int. J. Multiphase Flow* **1985**, *11*, 161.
[57] D. Barnea, *Int. J. Multiphase Flow* **1987**, *13*, 1.
[58] S. Mueller, E. W. Llewellin, H. M. Mader, *Proc. R. Soc. London, Ser. A* **2009**, *466*, 1201.
[59] E. Guazzelli, O. Pouliquen, *J. Fluid Mech.* **2018**, *852*, 852.
[60] S. M. Bhagwat, A. J. Ghajar, *Exp. Therm. Fluid Sci.* **2012**, *39*, 213.

How to cite this article: R. L. Höhn, A. Arabi, S. V. V. Ballesta, P. J. Sassi, J. Pallarès, Y. Stiriba, *Can. J. Chem. Eng.* **2025**, *103*(9), 4513. https://doi.org/10.1002/cjce.25663

APPENDIX A: EXAMPLE OF LIQUID AND SLURRY HOLDUP MEASURED

TABLE A1 Example OF liquid and slurry holdup measurements for fixed liquid superficial velocity of 0.75 m/s.

Gas superficial velocity (m/s)	Solid concentration	1st measurement Hl or Hls	2nd measurement Hl or Hls	3rd measurement Hl or Hls	4th measurement Hl or Hls	5th measurement Hl or Hls	Average value	Standard deviation	Flow pattern
0.2	Two-phase	0.905	0.907	0.850	0.800	0.832	0.859	0.042	Slug
	$C_s = 5\%$	0.882	0.830	0.860	0.927	0.902	0.880	0.033	Slug
	$C_s = 10\%$	0.831	0.837	0.824	0.859	0.869	0.844	0.017	Slug
	$C_s = 20\%$	0.894	0.858	0.834	0.799	0.874	0.852	0.033	Slug
1.5	Two-phase	0.410	0.525	0.485	0.472	0.360	0.450	0.058	Slug
	$C_s = 5\%$	0.562	0.425	0.452	0.258	0.436	0.427	0.097	Slug
	$C_s = 10\%$	0.350	0.370	0.345	0.398	0.364	0.366	0.019	Slug
	$C_s = 20\%$	0.629	0.505	0.448	0.360	0.621	0.513	0.103	Churn
7	Two-phase	0.282	0.325	0.197	0.270	0.208	0.256	0.048	Churn
	$C_s = 5\%$	0.307	0.192	0.287	0.242	0.284	0.262	0.041	Churn
	$C_s = 10\%$	0.316	0.213	0.203	0.286	0.256	0.255	0.043	Churn
	$C_s = 20\%$	0.352	0.251	0.303	0.253	0.258	0.283	0.039	Churn

TABLE A2 Assessment of existing liquid holdup models and the proposed model with the data of the literature by different flow patterns.

Two-phase flow												
	Cap-slug (3 test conditions)			**Slug (48 test conditions)**			**Churn (11 test conditions)**			**Dispersed bubble (4 test conditions)**		
	APD	**AAPD**	**RMSDP**	**APD**	**AAPD**	**RMSDP**	**APD**	**AAPD**	**RMSDP**	**APD**	**AAPD**	**RMSDP**
Nicklin[18]	−1.68	1.68	2.14	−4.58	7.51	9.43	−5.54	6.66	8.93	−3.09	3.09	3.64
Chisholm[19]	−20.16	20.16	20.20	−7.52	12.52	13.62	25.57	25.57	28.26	−19.32	19.32	19.33
Rouhani and Axelsson[20]	−1.68	1.68	2.14	−4.59	7.51	9.44	−5.73	6.66	9.00	−3.09	3.09	3.64
Bonnecaze et al.[21]	−1.68	1.68	2.14	−4.58	7.51	9.43	−5.55	6.67	8.93	−3.09	3.09	3.64
Beggs and Brill[22]	−3.94	3.94	4.34	−8.07	10.24	12.51	−10.35	10.49	14.15	−5.14	5.14	5.82
Huq and Loth[23]	−3.13	3.13	3.49	−4.07	7.45	8.62	3.36	7.16	8.00	−4.23	4.23	4.74
Woldesemayat and Ghajar[16]	−9.93	9.93	9.96	−10.21	12.20	14.26	−0.14	7.77	8.92	−13.48	13.48	13.90
Armand—Massena	−2.27	2.27	2.73	−7.74	9.10	11.02	−10.48	10.48	12.24	−3.44	3.44	4.01
Kanizawa and Ribatski[24]	−59.92	59.92	59.93	−75.94	75.94	76.17	−83.61	83.61	83.64	−64.70	64.70	65.04
Almabrok et al.[25]	−3.62	3.62	4.02	−16.47	17.03	19.54	−41.22	41.22	41.90	−4.84	4.84	5.50
AlSaif and Al-Sarkhi[26]	−1.52	1.52	1.87	−5.38	9.01	11.87	−25.60	25.60	26.82	−3.57	3.57	4.17
Three-phase flow with 5% of solid concentration												
	Cap-slug (3 test conditions)			**Slug (39 test conditions)**			**Churn (12 test conditions)**			**Dispersed bubble (2 test conditions)**		
	APD	**AAPD**	**RMSDP**	**APD**	**AAPD**	**RMSDP**	**APD**	**AAPD**	**RMSDP**	**APD**	**AAPD**	**RMSDP**
Nicklin[18]	−2.96	2.96	2.98	−6.40	10.39	12.65	0.35	13.94	16.69	−3.18	3.18	3.37
Chisholm[19]	−21.13	21.13	21.14	−7.47	13.70	16.96	35.51	38.61	43.78	−20.32	20.32	20.35
Rouhani and Axelsson[20]	−2.96	2.96	2.98	−6.41	10.40	12.65	0.12	13.85	16.60	−3.18	3.18	3.37

(Continues)

TABLE A2 (Continued)

Three-phase flow with 5% of solid concentration												
	Cap-slug (3 test conditions)			Slug (39 test conditions)			Churn (12 test conditions)			Dispersed bubble (2 test conditions)		
	APD	AAPD	RMSDP	APD	AAPD	RMSDP	APD	AAPD	RMSDP	APD	AAPD	RMSDP
Bonnecaze et al.[21]	−2.96	2.96	2.98	−6.40	10.40	12.65	0.34	13.94	16.69	−3.18	3.18	3.37
Beggs and Brill[22]	−5.20	5.20	5.25	−9.54	13.43	15.73	−3.46	15.51	18.28	−4.39	4.39	4.55
Huq and Loth[23]	−4.40	4.40	4.42	−5.41	10.06	12.05	9.51	17.08	19.90	−4.08	4.08	4.24
Woldesemayat and Ghajar[16]	−11.08	11.08	11.09	−11.50	15.20	17.36	7.19	18.59	21.53	−11.86	11.86	11.90
Armand—Massena	−3.55	3.55	3.57	−9.57	12.07	14.00	−5.32	12.45	15.65	−3.40	3.40	3.58
Kanizawa and Ribatski[24]	−64.42	64.42	64.43	−79.88	79.88	80.08	−84.85	84.85	84.92	−62.89	62.89	62.89
Almabrok et al.[25]	−4.89	4.89	4.93	−18.97	19.83	22.39	−40.04	40.04	40.81	−4.21	4.21	4.37
AlSaif and Al-Sarkhi[26]	−2.80	2.80	2.82	−7.76	11.27	14.61	−21.99	22.61	25.98	−3.43	3.43	3.59

Three-phase flow with 10% of solid concentration										
	Cap-slug (2 test conditions)			Slug (14 test conditions)			Churn (10 test conditions)			Cap-dispersed (1 test condition)
	APD	AAPD	RMSDP	APD	AAPD	RMSDP	APD	AAPD	RMSDP	APD
Nicklin[18]	1.55	1.55	1.80	−5.35	10.91	13.72	−7.07	13.03	15.23	2.07
Chisholm[19]	−17.15	17.15	17.15	−6.59	18.84	21.89	22.19	25.52	33.47	−16.09
Rouhani and Axelsson[20]	1.55	1.55	1.80	−5.37	10.91	13.72	−7.26	12.90	15.21	2.07
Bonnecaze et al.[21]	1.55	1.55	1.80	−5.36	10.91	13.72	−7.07	13.03	15.23	2.07
Beggs and Brill[22]	−0.41	0.64	0.76	−7.58	14.78	17.04	−11.87	16.56	17.95	0.69
Huq and Loth[23]	0.23	0.77	0.80	−4.69	11.91	14.57	0.72	13.89	14.26	1.06
Woldesemayat and Ghajar[16]	−7.24	7.24	7.30	−9.56	17.35	19.38	−2.69	17.42	17.99	−7.05
Armand—Massena	1.09	1.09	1.36	−8.88	11.96	14.16	−11.87	12.35	16.62	1.81
Kanizawa and Ribatski[24]	−67.46	67.46	67.46	−81.88	81.88	82.09	−88.54	88.54	88.56	−66.31
Almabrok et al.[25]	−0.13	0.68	0.69	−18.40	18.40	21.29	−41.30	41.30	41.91	0.89
AlSaif and Al-Sarkhi[26]	1.53	1.53	1.84	−5.99	11.30	14.75	−25.95	25.95	27.64	1.84

Three-phase flow with 20% of solid concentration										
	Cap-slug (2 test conditions)			Slug (12 test conditions)			Churn (14 test conditions)			Cap-dispersed (1 test condition)
	APD	AAPD	RMSDP	APD	AAPD	RMSDP	APD	AAPD	RMSDP	APD
Nicklin[18]	3.94	3.94	4.63	−8.62	8.87	10.17	−17.21	17.28	19.28	0.82
Chisholm[19]	−14.88	14.88	14.98	−13.43	13.43	14.71	7.14	12.47	16.43	−16.84
Rouhani and Axelsson[20]	3.94	3.94	4.63	−8.63	8.88	10.18	−17.35	17.38	19.38	0.82
Bonnecaze et al.[21]	3.94	3.94	4.63	−8.63	8.87	10.17	−17.22	17.28	19.29	0.82
Beggs and Brill[22]	1.94	2.11	2.87	−12.03	12.28	13.65	−19.31	19.76	22.41	−0.55
Huq and Loth[23]	2.59	2.59	3.44	−8.86	8.86	9.77	−10.75	12.00	13.66	−0.18
Woldesemayat and Ghajar[16]	−5.01	5.01	5.55	−14.87	14.87	16.25	−13.30	14.81	17.51	−8.16
Armand—Massena	3.47	3.47	4.17	−11.26	11.36	12.64	−21.82	21.82	23.00	0.56

TABLE A2 (Continued)

Three-phase flow with 20% of solid concentration										
	Cap-slug (2 test conditions)			Slug (12 test conditions)			Churn (14 test conditions)			Cap-dispersed (1 test condition)
	APD	AAPD	RMSDP	APD	AAPD	RMSDP	APD	AAPD	RMSDP	APD
Kanizawa and Ribatski[24]	−79.17	79.17	79.17	−89.44	89.44	89.53	−94.01	94.01	94.02	−79.03
Almabrok et al.[25]	2.22	2.22	3.10	−18.05	18.05	20.08	−45.44	45.44	46.29	−0.35
AlSaif and Al-Sarkhi[26]	3.93	3.93	4.67	−8.82	9.59	11.50	−30.10	30.10	32.36	0.59

Abbreviations: AAPD, average absolute percentage difference; APD, average percentage difference; RMSPD, root mean square percentage difference.